COO-3522-2

ANNUAL PROGRESS REPORT

TO

THE UNITED STATES ATOMIC ENERGY COMMISSION

CONTRACT AT (11-1)-3522

BIOLOGICAL AND CLINICAL DOSIMETRY

Contract Period:	November 1, 1972 - October 31, 1973
Report Period:	July 1, 1972 - June 30, 1973
Senior Investigator:	John S. Laughlin, Ph.D., Member
Co-Investigators:	Thomas R. Canada, Ph.D., Associate
	John F. Detko, M.A., Research Associate
	Joseph C. McDonald, M.S., Research Physicist

Sloan - Kettering Institute for Cancer Research
410 East 68th Street, New York, N. Y. 10021

DISCLAIMER

Page

TABLE OF CONTENTS

I. SUMMARY

Detailed studies have been made of the collimated neutron fields produced in the $^{9}Be(d,n)^{10}B$ and the $^{9}Be(^{3}He,n)^{11}C$ reactions, using the 8 MeV deuteron and 25 MeV ^{3}He beams obtained from the MSKCC isochronous cyclotron. The properties which have been studied include: the angular distribution of the total dose, the attenuation properties of various materials and the depth dose behavior of the total dose, the gamma ray dose, and the neutron fluence. Isodose distributions have been obtained and used to calculate preliminary treatment plans. Distributions of the dose in LET have been obtained at a number of points within the fields and used in the interpretation of some radiobiological studies.

A tissue equivalent calorimeter system has been assembled. Preliminary results and the attending problems are discussed.

Detailed dosimetry studies of ^{252}Cf have been conducted. Neutron and gamma ray absorbed dose distributions have been measured and preliminary estimates of the beta ray dose are discussed. Preliminary results of a series of rabbit testes irradiations are also given.

Further evaluation tests were performed on the prototype orthogonal strip, ultra pure germanium camera. The camera detector area is 4 cm^2. Tests with a point source of ^{57}Co(122, KeV) and ^{99m}Tc(140 KeV) phantom demonstrated that the scintillation type cameras cannot match the 4mm spatial resolution of the germanium camera obtained with in-vivo tests on small mammalian organs. In initial stability tests, the germanium camera displayed no ill effects in several cyclings between room temperature and liquid nitrogen. Some deterioration occurred when the cryostat was opened to air.

Ultra pure germanium diodes with boron implanted p^{+} contacts were constructed from 5 cm diameter material using "in house" facilities. The diodes were evaluated for use in fabrication of an orthogonal strip matrix.

A square (10 x 10) orthogonal strip matrix of (3.25 x 3.25)cm^2 area and nearly 9mm thickness has been constructed and is operational. A single such unit increases the area of the gamma camera detector to almost 11 cm^2 with around 3mm spatial resolution. Measurements of ^{57}Co(122 KeV) show an energy resolution (FWHM) of 4 KeV. Tests on stability, electrical and image characteristics, have begun.

II. PHYSICAL PROPERTIES OF THE MSKCC CYCLOTRON PRODUCED FAST NEUTRON FIELDS

(T.R. Canada, J.C. McDonald, A. Mittleman, and J.S. Laughlin)

A. Introduction

With the hope of improvement in therapeutic response through the use of high linear energy transfer radiation, a number of fast neutron therapy projects have been or are presently being developed. The programs presently underway in the United States are connected with cyclotron installations which were originally designed for nuclear physics research and are in rather remote locations. These are large installations representing a major capital equipment investment. They require large and highly skilled operational staffs and relatively large operating budgets. Such installations are not feasible for wide scale application throughout the nation's hospitals because of the prohibitive expense. Should fast neutron radiotherapy prove to be a valuable addition to the present modalities of treating cancer, a more accessible and inexpensive source of neutrons would be required.

An alternative is to use a compact isochronous cyclotron to produce fast neutrons. The optimum size, and thus the potential neutron energy and dose rate produced by a cyclotron, involves many different factors. For application to all lesions encountered, an average neutron energy adequate to produce the 50% dose at a depth of 10 cm beyond the patient surface has been suggested (1). There are, however, commonly encountered lesion sites of importance which may be treated with sources whose depth dose characteristics do not meet this criterion. In fact, in the most extensive clinical trial to date (Hammersmith) a wide variety of tumor sites are being treated with a source whose 50% dose is at approximately 8 cm (2). The purpose of the present report is to describe the properties of several fast neutron fields produced using the Memorial Sloan-Kettering Cancer Center compact isochronous cyclotron, with a view to the possible radiotherapeutic use of these beams.

The fast neutron fields of principal interest here are those produced in the $^{9}Be(^{3}He,n)^{11}C$ and $^{9}Be(d,n)^{10}B$ reactions. Previous measurements of the neutron energy spectra generated by these reactions have shown them to be distinctively different (3,4). The ^{3}He induced spectrum shows a broad peak at approximately 7 MeV (a full width at half maximum of $\sim$9 MeV with a tail extending to approximately 26 MeV). The deuteron induced spectrum, on the other hand is strongly peaked at $\sim$3.5 MeV (FWHM=4 MeV) with a tail extending to $\sim$12 MeV. The differences in these spectra are clearly reflected in the data presented in Section C below. In Section B the experimental procedures used in this work are described.

B. Experimental Procedures

The overall system which may be thought of as constituting the neutron source has three important components, the characteristics of which determine the properties of the neutron field (see Figure 1). The first of these, the MSKCC isochronous cyclotron, is capable of extracting 200 μa beams of 25 MeV ^{3}He or 8 MeV deuterons, and 100 μa of 15 MeV protons. The external beam handling system includes quadrupole and steering magnets which allow the beam to be focused and centrally positioned on the target.

The second important component, the target system (Figure 1), consists of a thick beryllium plate, an electron suppressing ring, a beam collimator, and a water cooling channel. The tantalum collimator restricts the beam to a circle (2.54 cm in diameter) centered on the 0.508 cm thick beryllium plate. Studies of the target beam current as a function of the suppression voltage showed a minimum in the current at voltages greater than -20 volts. This minimum was approximately 6% less than the intensity measured when no suppression was present. A suppressor voltage of -50 volts was routinely used. The beam current was monitored at the cyclotron control console with a current digitizer which simultaneously displayed the integrated charge and the beam current. The measurements reported here were normalized to one or the other of these parameters. The sheet of chilled water which flows at the rate of 3 gals. per minute across the back face of the plate was necessary to dissipate the power of more than 1.2 kilowatts delivered by the beam. Even with this cooling, the target plates have shown small hair-line flaws when exposed to repeated rapid temperature changes.

The third important component of the neutron source used in these studies is the collimation system. This system was designed as a prototype, which would allow general dosimetry and biological experiments to continue while studies of the proper material composition and physical dimensions necessary for a final system design were also carried out. The collimator had an overall length of 40 cm; 10 cm of steel, 5 cm of lead and 25 cm of a polyethylene-lead-boron mixture* (80% lead, 1% boron by weight). It defined a circular field with a diameter at the exit surface of either 5 or 8 cm.

A number of measuring devices were used to determine the properties of the neutron fields produced using this system. Dose measurements were made with three ionization chambers; (Figure 2) two of which were constructed of tissue equivalent (T.E.) plastic (Shonka A-150) and were filled with a T.E. gas (66% CH_4, 31% CO_2,

*Obtained from Reactor Experiments, San Carlos, California.

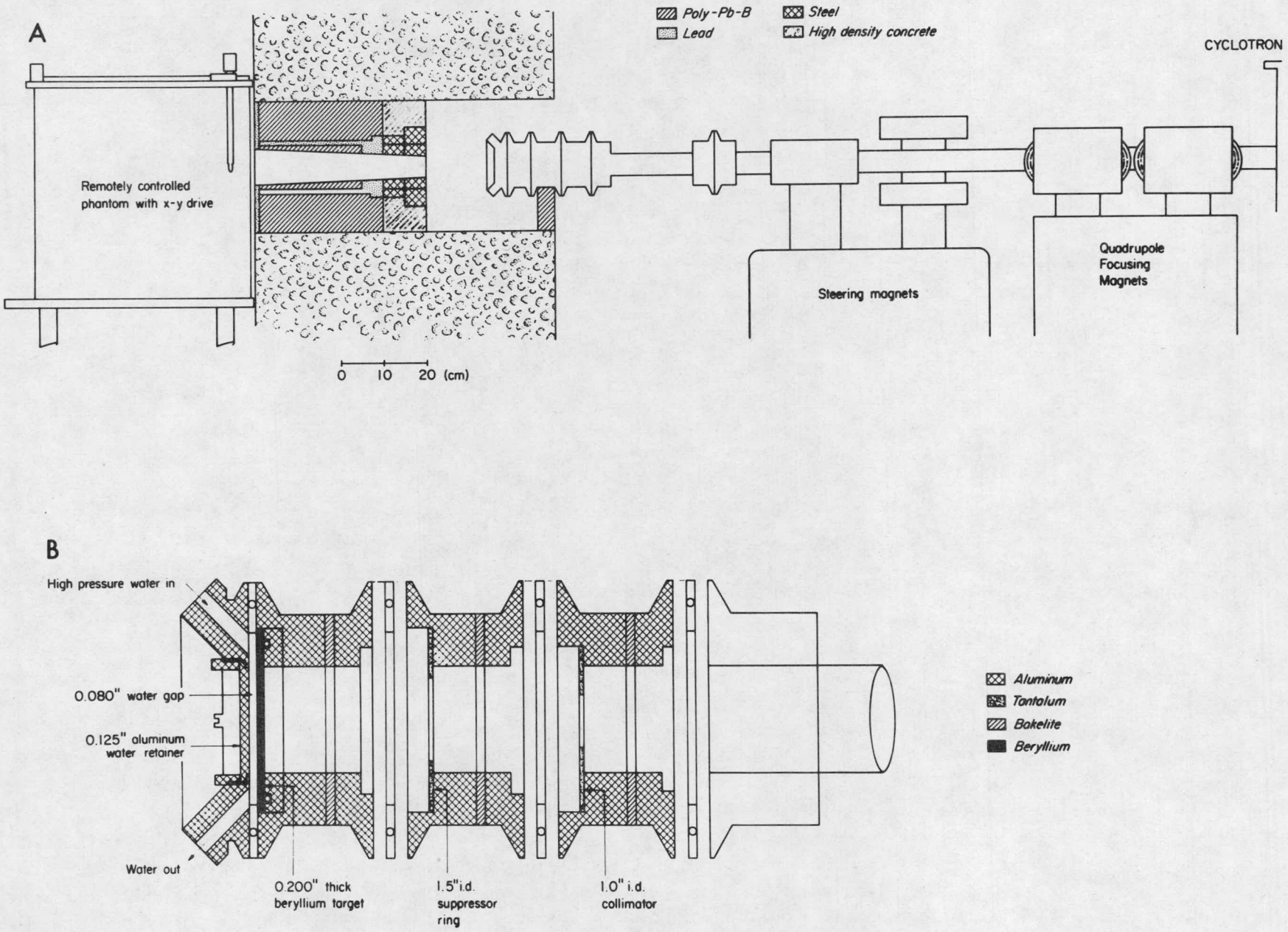

Figure 1. (a) Schematics of the cyclotron: fast neutron facility and (b) Beryllium target assembly

3% N_2). These were sensitive to the total (neutron plus gamma ray) dose. The larger of the two (Figure 2b) has a cylindrical active volume (1.0 cc) with a radius of 1 cm, and a plate spacing of 0.2 cm. The second (Figure 2c) was used when higher spatial resolution was required. This chamber is thimble shaped with an active volume of 0.05 cc. The third (Figure 2d) chamber has physical dimensions identical to those of the thimble chamber but was constructed of aluminum and filled with argon. This chamber, which has a very small sensitivity to neutrons ($\sim$2%), was used to determine the component of the dose arising from gamma rays. Either the ionization current or the integrated charge was measured with an electrometer (Keithly 602) which was equipped with a digital readout.

A portable gas handling system was used to fill the chambers and to monitor temperature and atmospheric pressure (see Figure 3). The system includes a fore-vacuum pump, a thermistor thermometer, a barometer, and a differential pressure gauge, which allowed pressure measurements to be made relative to the atmosphere or relative to a vacuum. It was used in the latter fashion when a spherical proportional counter, discussed below, was to be filled.

The ionization chambers are calibrated at fixed depths in a polystyrene phantom placed in a ^{60}Co gamma ray field. This ^{60}Co source is referenced to calibrations from the National Bureau of Standards. In order to apply the resulting calibration to measurements of dose arising in a neutron field it is necessary to calculate the average energy per ion pair expended by recoiling heavy particles as compared with electrons. This factor was determined to be 1.055 for the T.E. gas used here (5).

A tissue equivalent, 1.27 cm diameter proportional counter (Rossi-type) was used to measure linear energy transfer distributions (Figure 2a). Measurements were generally made with a T.E. gas pressure which gave an equivalent sphere size of 1 micron. Pulses from the counter were put through a preamp and a linear amplifier and stored in a 256 channel multichannel analyzer which is interfaced with an IBM 1800 computer. The resulting spectra were transmitted to the computer and were available for immediate analysis.

Neutron activation techniques were used to determine relative neutron planar fluences at various positions within the fields. Aluminum foils (1.27 cm diameter, 0.075 cm thick, 99.999% aluminum) and indium foils (1.27 cm diameter, 0.025 cm thick, 99.99% indium) were activated within 0.05 cm thick cadmium covers by the ^{27}Al (n,p) ^{27}Mg and the ^{115}In (n,n') ^{115m}In reactions respectively. ^{27}Mg β-decays to ^{27}Al with a 9.5 minute half-life giving rise to

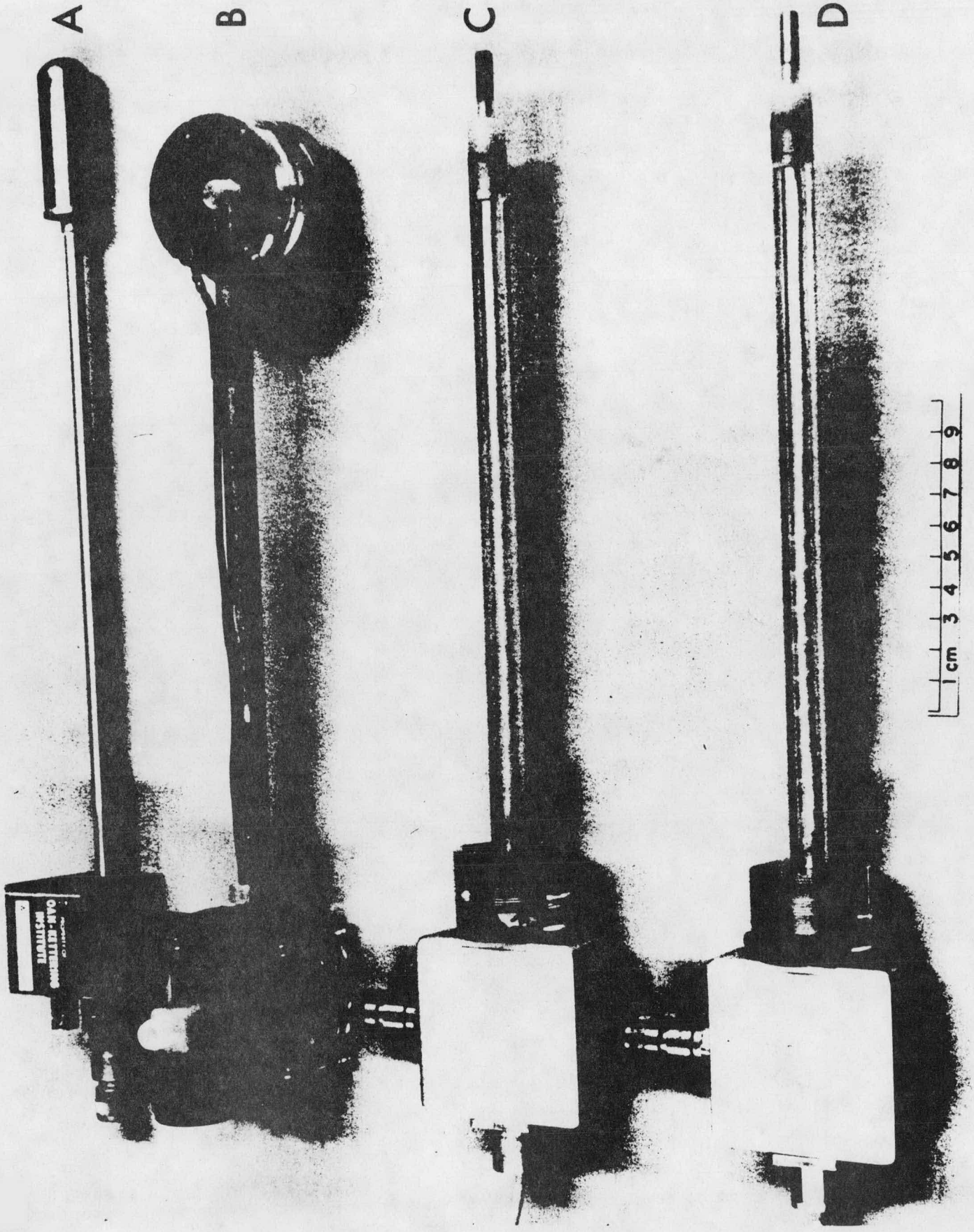

Figure 2. (A) 1.27 cm diameter spherical proportional counter.
(B) 1 c.c. planar T.E. ionization chamber.
(C) 0.05 c.c. thimble T.E. ionization chamber.
(D) 0.05 c.c. thimble aluminum ionization chamber.

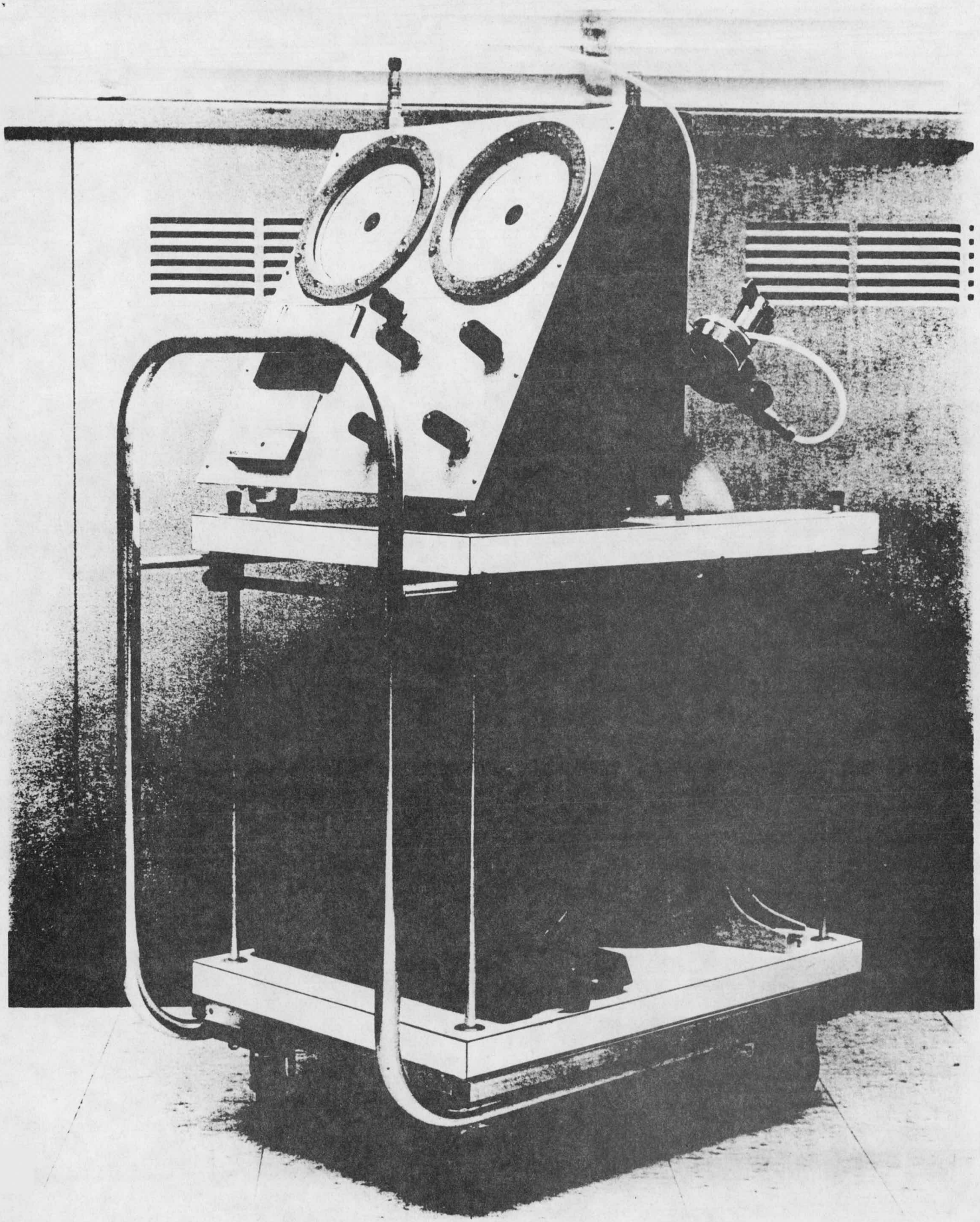

Figure 3. Portable gas handling system for filling ionization chambers and proportional counters.

gamma-rays at 0.842 and 1.013 MeV. Gamma-ray spectra were obtained using a 30 cc Ge(Li) detector and a 1024 channel multi-channel analyzer. An example of the spectra obtained from the aluminum foils is shown in Figure 4. The relative fluences were obtained by determing the areas under the 0.842 MeV photo peaks (a smoothed background was subtacted) and normalizing the data to equal irradiation and counting times. Because of the short half-life involved, a given aluminum foil was individually irradiated for approximately 20 minutes, during which time the preceding foil was counted.

The long half-life of the ^{115m}In, 4.4 hrs., allowed the simultaneous irradiation of a number of foils. The background arising from the decay of ^{116}In ($t_{\frac{1}{2}}$=54 min.) produced by neutron capture was large (see Figure 5). The foils were, therefore, not counted until at least 4 hrs. after irradiation. The spectra obtained after this time were much cleaner (Figure 5) and clearly showed the 0.335 MeV ^{115m}In decay.

Many of the measurements described below were made in a large (50x50x70 cm) polystyrene, water filled tank (Figure 6) whose front face was 4mm thick. A remotely controlled, two dimensional, track assembly, which was designed to support the ionization chambers, could be mounted on the tank top to facilitate isodose distribution measurements. The remote control allows positioning steps of 0.5 cm to 5 cm with an accuracy of better than 0.05 cm.

C. Results and Discussion

The important neutron field parameters which must be considered in the design of a collimation system include the neutron energy distribution as a function of angle, the variation of the field intensity with angle, and the dose attenuation properties of various materials. The neutron energy spectra produced by the (^3He,n), and (d,n) reactions on beryllium have been discussed above. The relative angular distribution of the total dose for these reactions is shown in Figure 7 . These distributions were measured with the 0.05 cc T.E. ionization chamber described above which was moved in 7.5° steps about the target at a 30 cm radius. The contribution to the total dose due to the gamma radiation arising both from the prompt and activation gamma rays at the target is expected to be less than 10% and to exhibit an isotropic distribution. Similarly any scattering from the room walls will be small and isotropic. Therefore, the angular distributions of the total dose reflect the behavior of the neutron component of the field plus a small isotropic

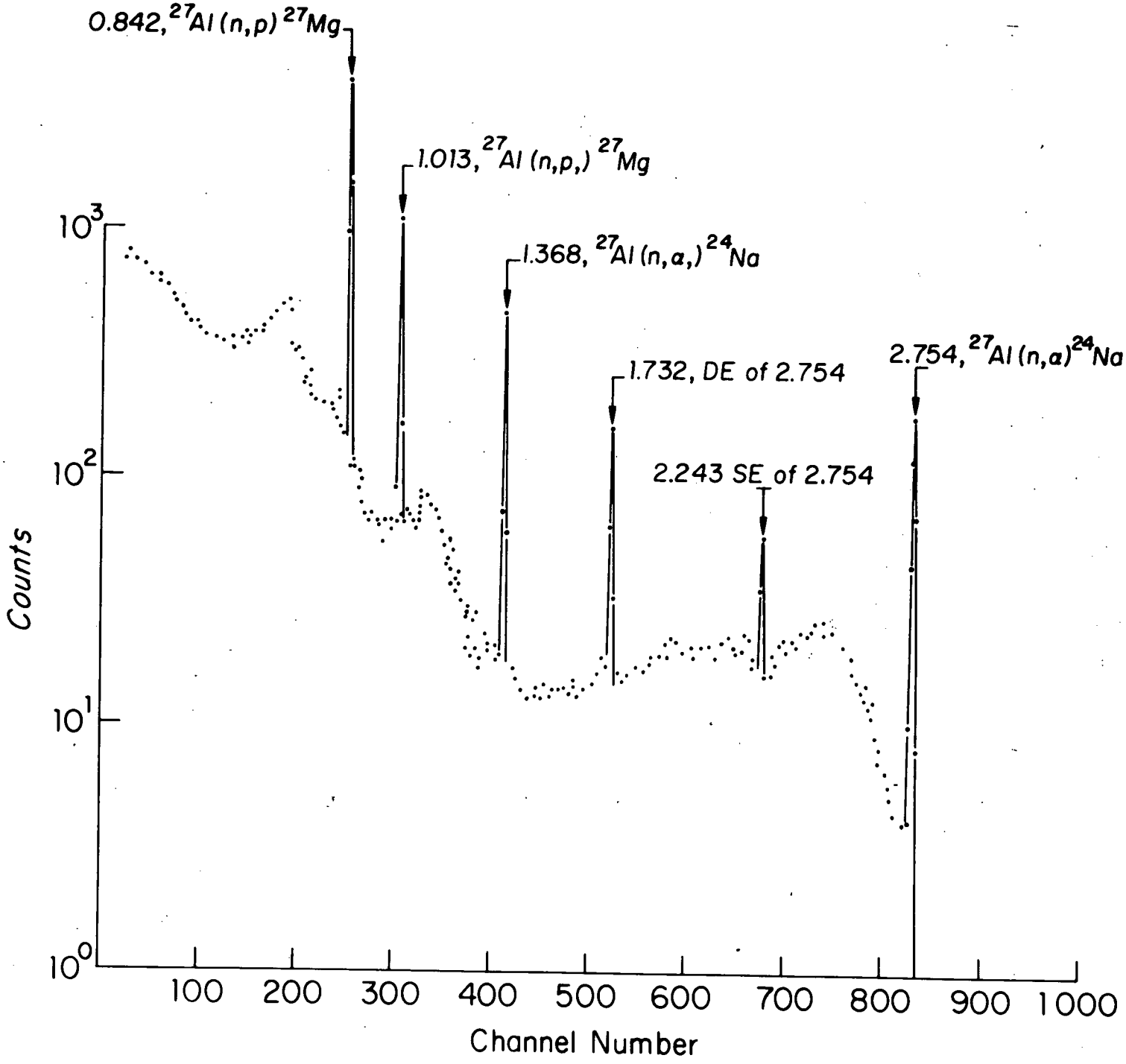

Figure 4. Gamma ray spectrum obtained from an activated aluminum foil.

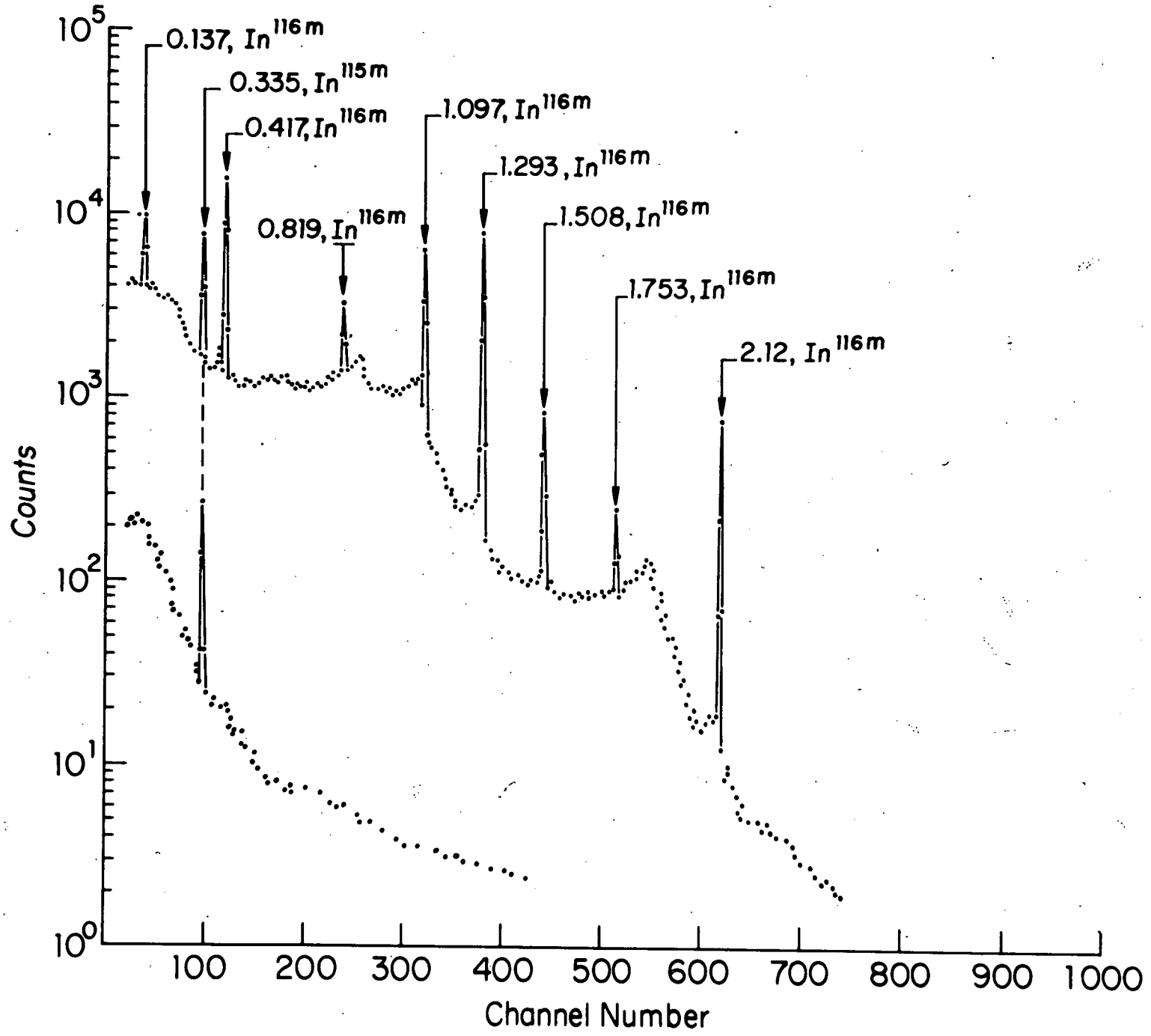

Figure 5. Gamma ray spectra obtained from an activated indium foil immediately after and 20 hours after irradiation.

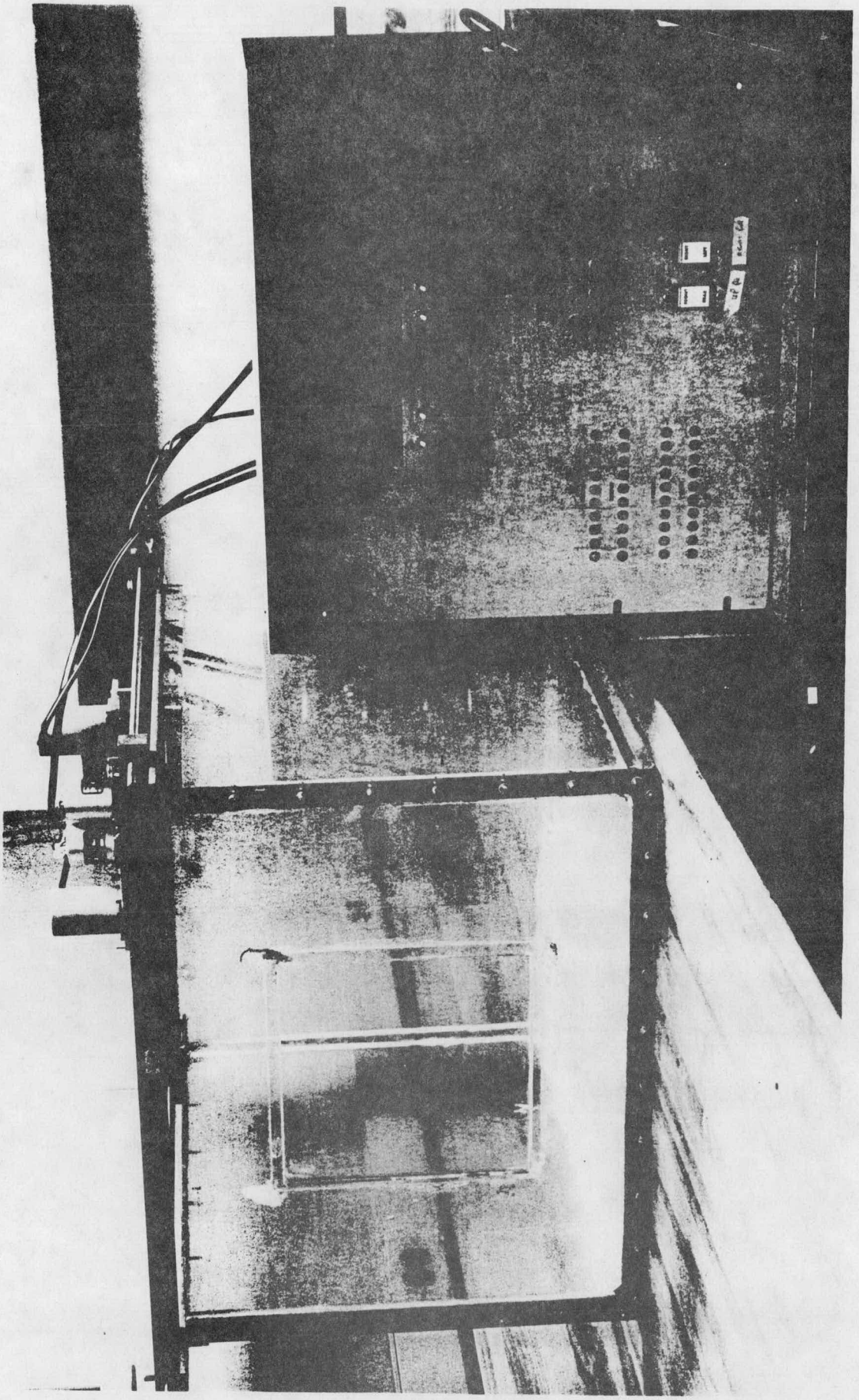

Figure 6. Polystyrene tank with x-y drive and remote control unit.

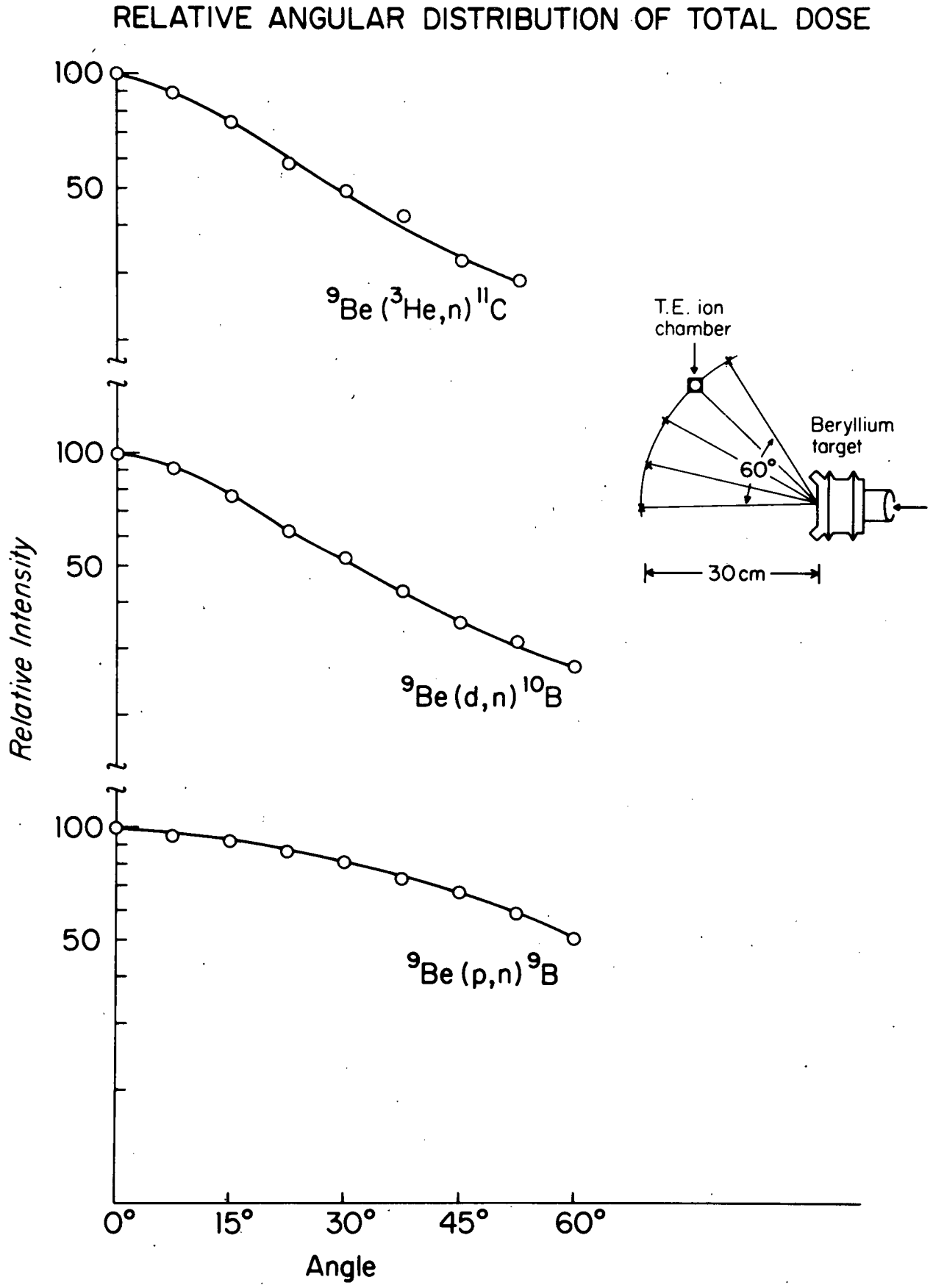

Figure 7. Relative angular distributions for three neutron producing reactions.

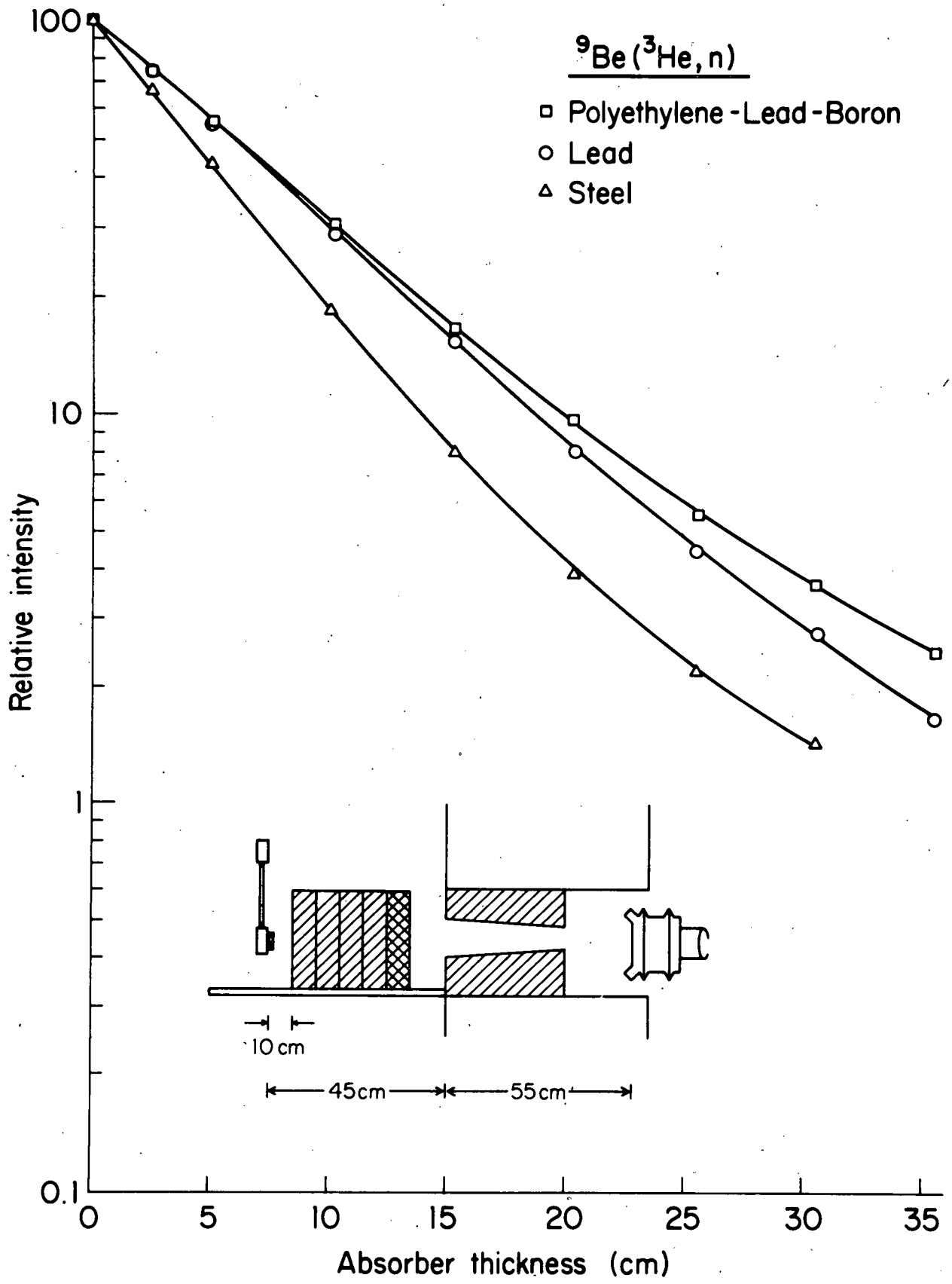

Figure 8. Dose attenuation curves for three materials in $^{9}Be(^{3}He,n)$ fast neutron field. A schematic of the experimental arrangement is shown.

component. The excellent agreement of $^{9}Be(d,n)$ distribution measured here with that of ref. (4) in which the neutron angular distribution was measured by time-of-flight techniques, indicates that the gamma ray and wall scatter components are negligible. The strong forward peaking of the ($^{3}He,n$) and (d,n) reactions suggests a large direct reaction component in the respective cross sections. Conversely, the relatively isotropic behavior at forward angles of the $^{9}Be(p,n)^{9}B$ reaction shown in Figure 7, suggests a large compound nucleus reaction component in its cross section. Forward peaked neutron fields have obvious advantages when collimation problems are to be considered.

Dose attenuation curves for the $^{9}Be(^{3}He,n)$ and $^{9}Be(d,n)$ fields were measured in the experimental arrangement shown schematically in Figure 8. The 1.0 cc T.E. ionization chamber was positioned 45 cm in front of an 8 cm diameter, collimated field. Steel, lead and polyethylene-lead-boron (80% Pb, 1% by weight) bricks (cross sectional dimensions of 10 x 20 cm) were placed between the collimator face and the ionization chamber. The initial brick was placed 10 cm in front of the ionization chamber. Additional bricks were added as shown in the figure. The results for the two fields and the three materials are summarized in Figures 8 and 9. All of the curves show a deviation from a purely exponential behavior at larger thickness which is due to scattering from the absorbing material and the room walls. These data show the superior attenuation properties of steel.

Figure 10 summarizes the results of some composite material measurements. In this case 25 cm of the polyethylene mixture (placed adjacent to the ionization chamber) was followed by up to 10 cm of steel or lead. These data show that the attenuation achieved by 30 cm of steel is equal to that achieved by 25 cm of the polyethylene mixture plus 5 cm of steel for the deuteron (or 10 cm for the ^{3}He) induced neutron field. Thus, an optimum collimator system for these fields does not have to include a large amount of heavy material such as steel or tungsten. A relatively small amount is adequate to degrade the average neutron energy to a region where light weight hydrogenous materials are effective.

The variation of the total dose with depth in water represents a fundamental parameter of interest for any given neutron field under study. Figure 11 shows the depth dose behavior for the deuteron and ^{3}He on beryllium fields measured at SSD's of 100 cm and 85 cm respectively. The measurements were made with the 0.05 cc T.E. chamber in the water tank which was placed either 25 cm (for the ^{9}Be+d field) or 10 cm (^{9}Be+^{3}He field) in front of the 5 cm diameter collimator. These collimator to surface distances (CSD) were necessary because of space considerations. The representations

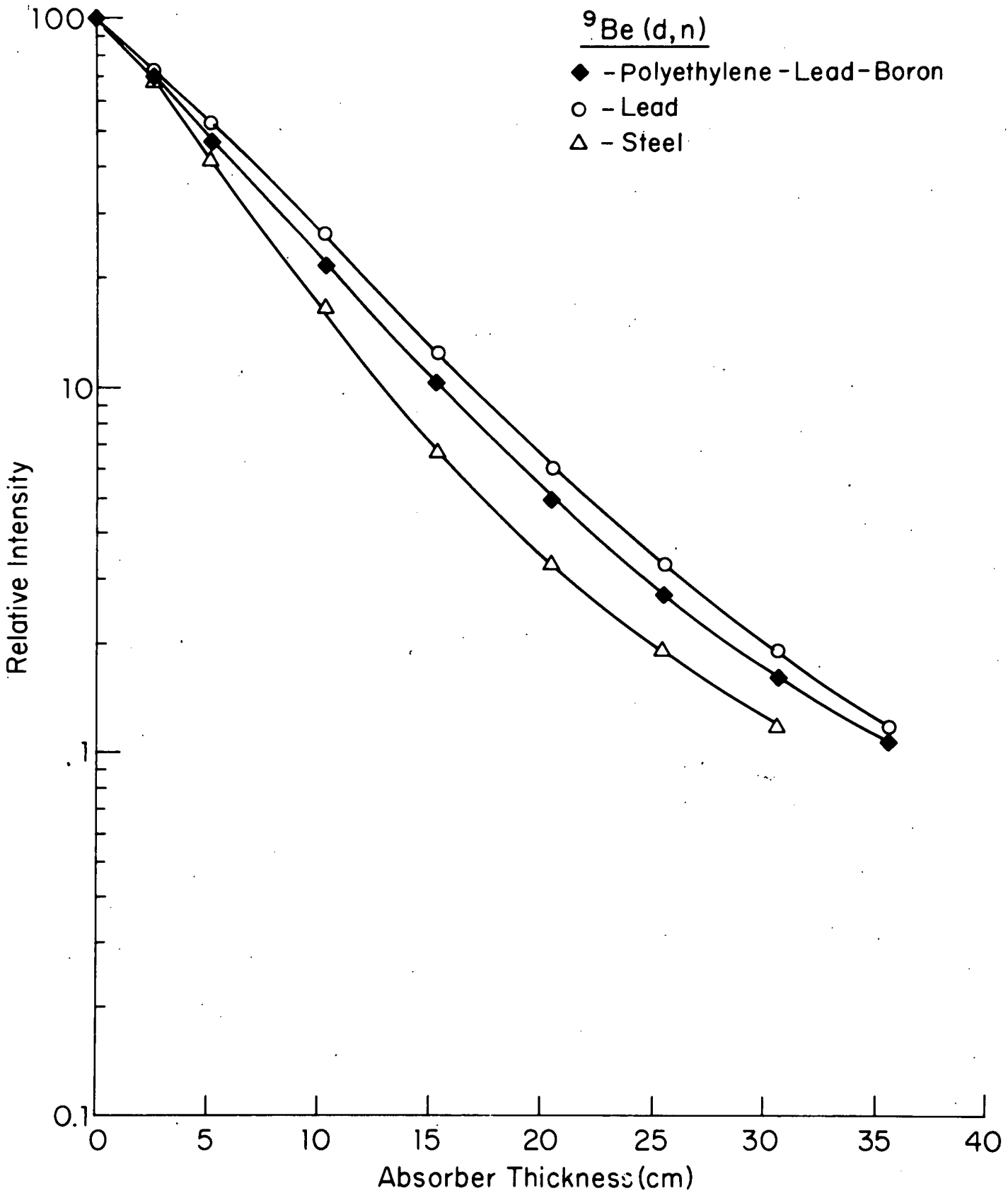

Figure 9. Dose attenuation for three materials in ^{9}Be(d,n) fast neutron field.

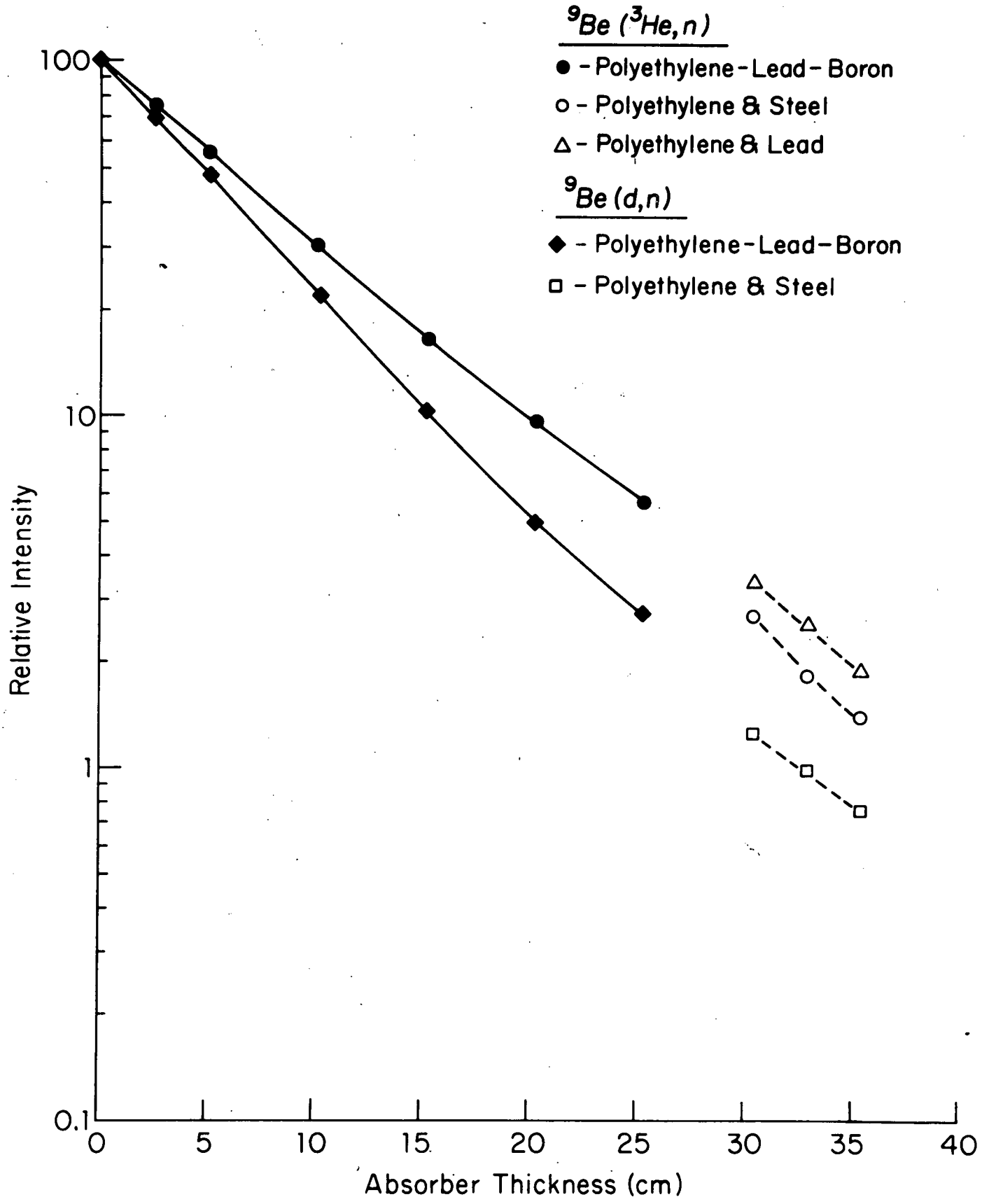

Figure 10. Dose attenuation curves for some composites of materials in $^{9}Be(^{3}He,n)$ and $^{9}Be(d,n)$ fast neutron fields.

of the dose between the surface and 0.8 cm in Figure 11 are approximate extrapolations. The half value depths are 6.5 cm and 7.2 cm for the deuteron and ^{3}He induced fields respectively. The corresponding dose rates at the surface for these geometries are 7.5 (^{3}He) and 13 (d) rads/100 μa-min. For comparison the depth dose measured at the Hammersmith cyclotron for a ^{9}Be+d (E_d=16 meV), 6x4 cm field is also shown in Figure 11. With an SSD of 120 cm, the penetrability of the Hammersmith field is only slightly better than that of the ^{9}Be+^{3}He field at an SSD of 85 cm (2).

The components of the total dose arising from gamma rays and neutrons as a function of depth have been studied in detail. The results are summarized in Figure 12. The solid lines labeled "Total Dose" and "Gamma Dose" were measured using the .05 cc T.E. and the .05 cc aluminum (argon filled) ionization chambers respectively. The gamma-ray dose is plotted as a percentage of the total dose at the surface. It is larger for the ^{3}He induced field and increases relative to the total dose as a function of depth for both the ^{3}He and deuteron induced fields.

The data points show the variation of the neutron planar fluence as determined using two sets of activation foils. The threshold for the ^{115}In(n,n')^{115m}In reaction is at approximately 1 MeV. The reaction cross section rises rapidly and has a reasonable value (200 mb) up to at least 10 MeV. Therefore, the data from these foils, shown as open circles, approximate the behavior of the total neutron spectrum. The fact that the neutron fluence drops off faster with depth than does the total dose is due to the increasing gamma-ray contamination. The ^{27}Al(n,p)^{27}Mg cross section increases slowly from approximately 4 MeV and reaches a peak between 11 and 13 MeV. The relative neutron fluences measured with these foils (the solid data points) show the behavior of the higher energy portions of the neutron energy distributions. The divergence of the aluminum and indium activation data indicate an increase in the average neutron energy with increasing depth in water.

Similar data, obtained along a line 4 cm in front of the 8 cm diameter prototype collimator, are shown in Figure 13. The total dose in air (the dashed line) was measured with the 0.05 cc T.E. chamber and is compared in the figure with the relative neutron fluences determined using the indium foils. The approximation, that these activation data represent the behavior of the total neutron fluences, is less valid here than it was in the discussion above. Large differences between the central axis and penumbra

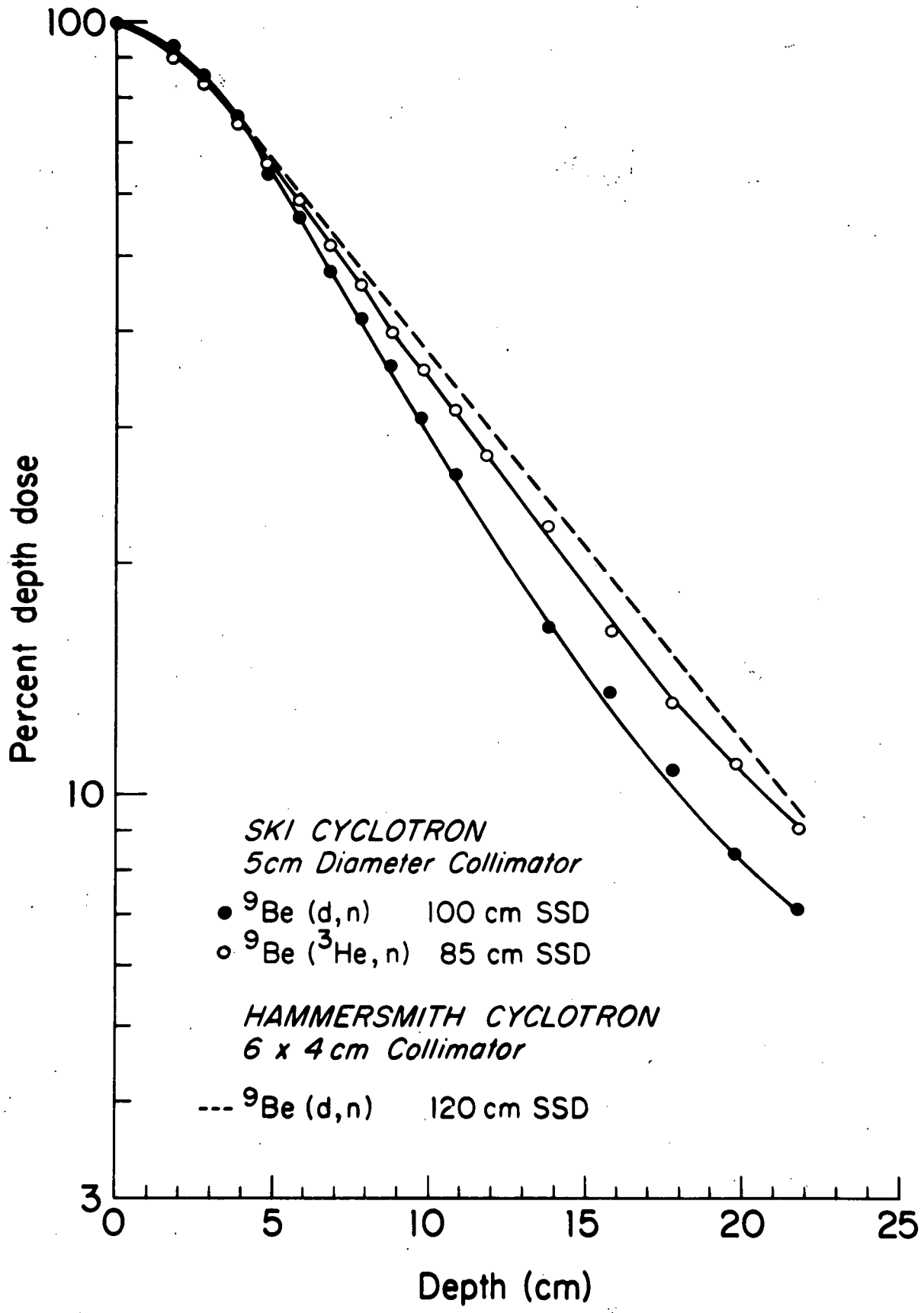

Figure 11. Depth dose curves measured for the collimated fast neutron fields produced by the SKI cyclotron compared with that obtained in the ^{9}Be(d,n) reaction at the Hammersmith cyclotron. The latter includes only that part of the total dose arising from neutrons.

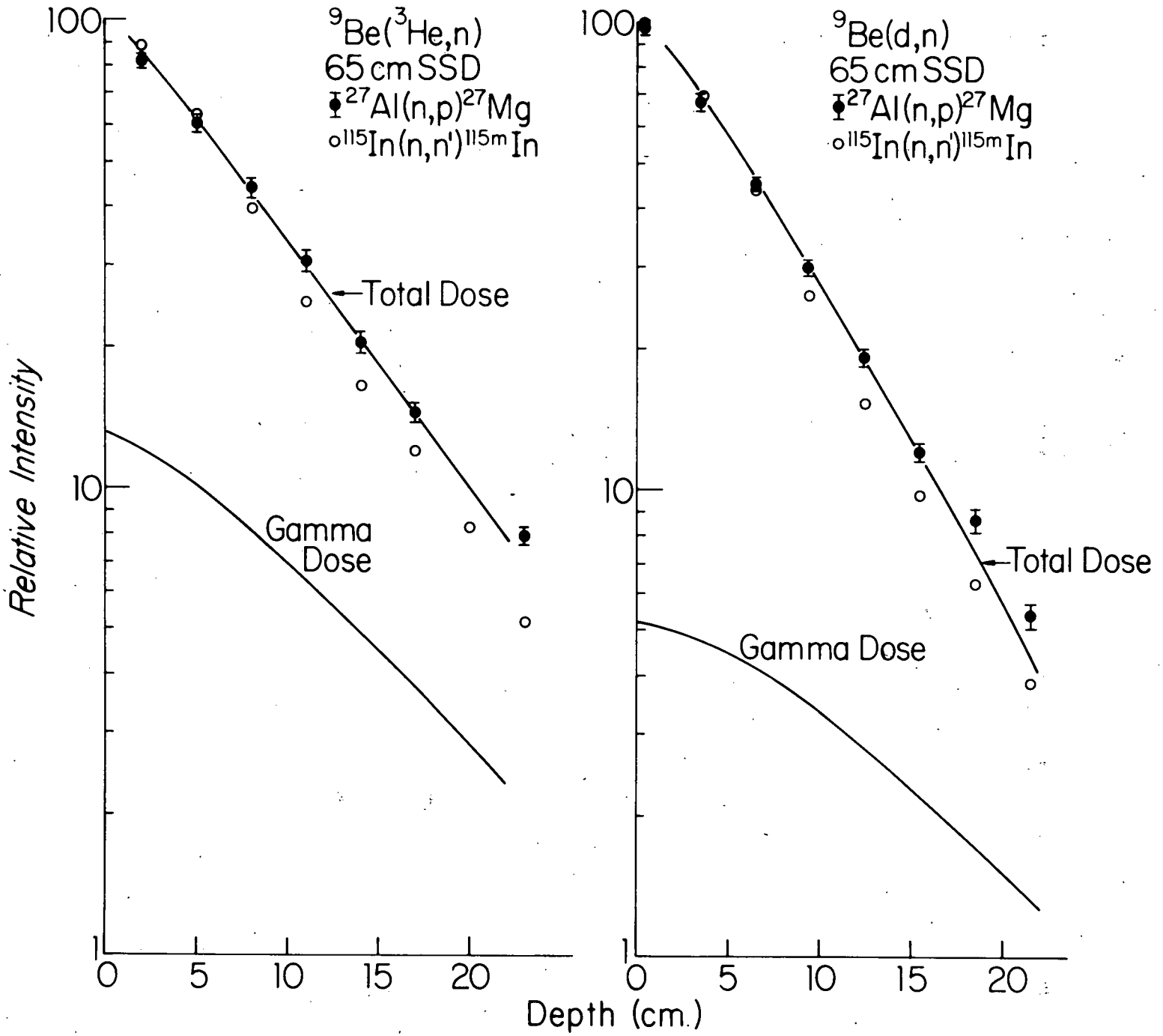

Figure 12. Total dose, gamma dose, and relative neutron planar fluence as functions of depth in water for an 8 cm collimated field.

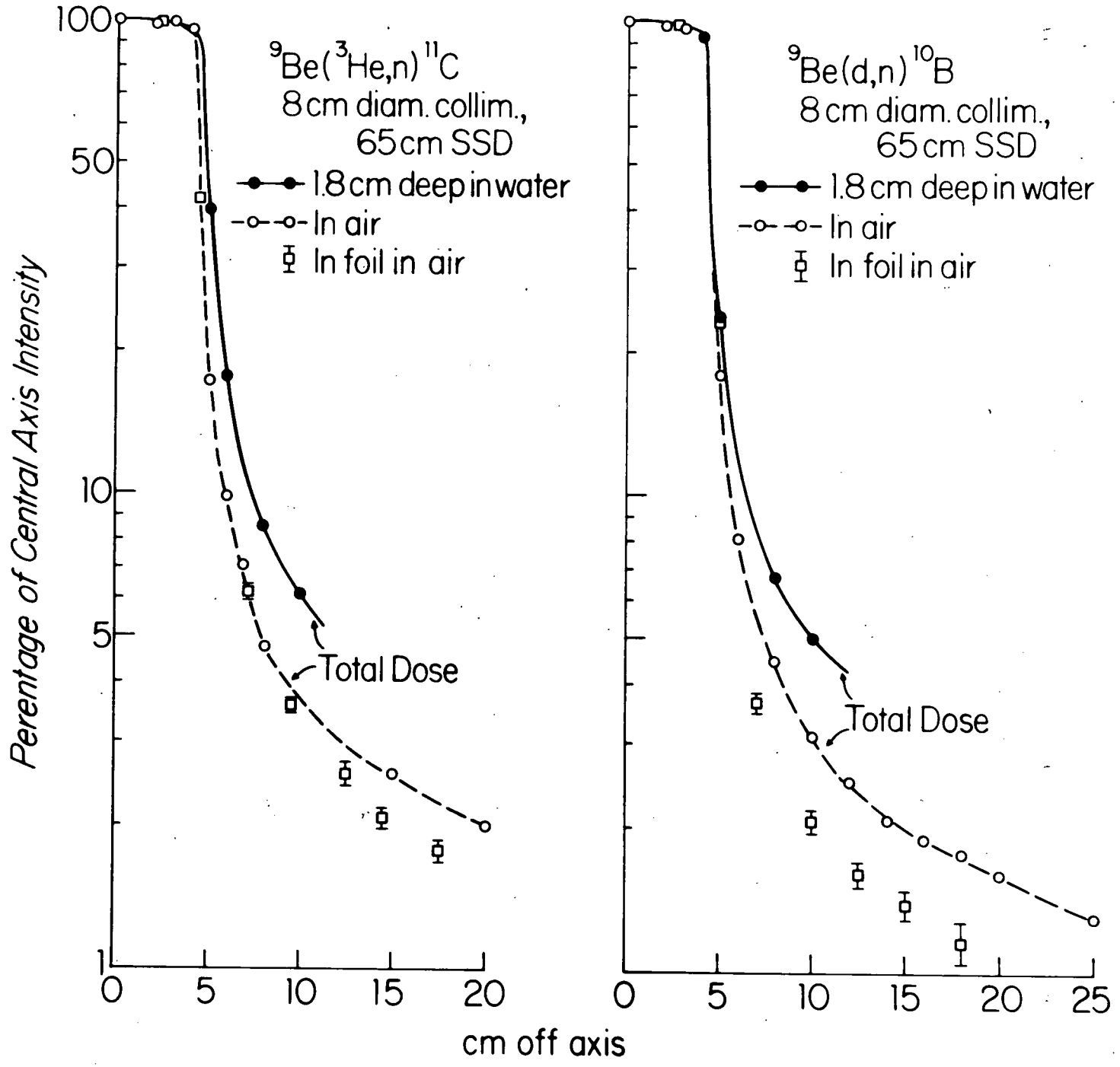

Figure 13. Relative dose in water, in air, and relative neutron fluence as functions of position across the collimated 8 cm diameter neutron fields.

neutron energy distributions will directly influence the results. Nevertheless, the differences between the total dose curves and the activation data are, to first order, directly proportional to the gamma ray dose. The differences between the "in-air" and the 1.8 cm depth "in-water" total dose curves are due to scatter within the water phantom. A final collimator design will require that this latter difference be large relative to the total dose measured in air.

Examples of the isodose distributions obtained with this prototype collimator (a nominal 5 cm field) are shown for the deuteron and ^{3}He induced fields in Figure 14. These were measured in the water tank described above at SSD's of 100 cm (CSD=25 cm) and 85 cm (CSD=10 cm) respectively.

Such distributions have been used to make preliminary treatment dose distribution calculations (using an Artronix PC-12 mini-computer) for selected anatomical sites; i.e. extremities, upper thorax, head and neck, and the chest wall (6). As an example, treatment plans for epidermoid carcinoma of the larynx are shown in Figures 15 and 16. Neutron tissue equivalent bolus material is used in Figure 15 to create a "wedged pair". The resulting distribution shows a 5% dose gradient in the target volume and spinal cord doses well below accepted tolerance levels. An alternate plan, using parallel-opposed, bolused fields (Figure 16) lowers the dose to the spinal cord, while increasing the target dose gradient to approximately 10%. Both of these plans are comparable to the cobalt-60 wedged pair (Figure 17) and further improvement is expected with optimizations of the collimation system and the geometry; i.e. a reduction in the CSD.

Simple total dose characterizations of high linear energy transfer (LET) radiation fields are inadequate to describe the observed radiobiological response of systems exposed to them. This response is found to have a strong dependence upon the LET of the radiation. In the case of a fast neutron field, the dose is deposited by charged secondary particles which have a large range of LET values.

In hydrogenous materials, neutrons in the energy range of interest here (E_n <10 MeV) lose their energy primarily by scattering with protons. The recoil protons have a minimum LET, depending upon the maximum energy available (<10 keV/μ), and a maximum LET ($\sim$90 keV/μ) at the Bragg peak. Similar behavior is exhibited by alpha particles, produced in (n,α) reactions, which have a maximum LET at the end of their track of approximately 220 keV/μ. Heavier reaction products and recoiling nuclei are

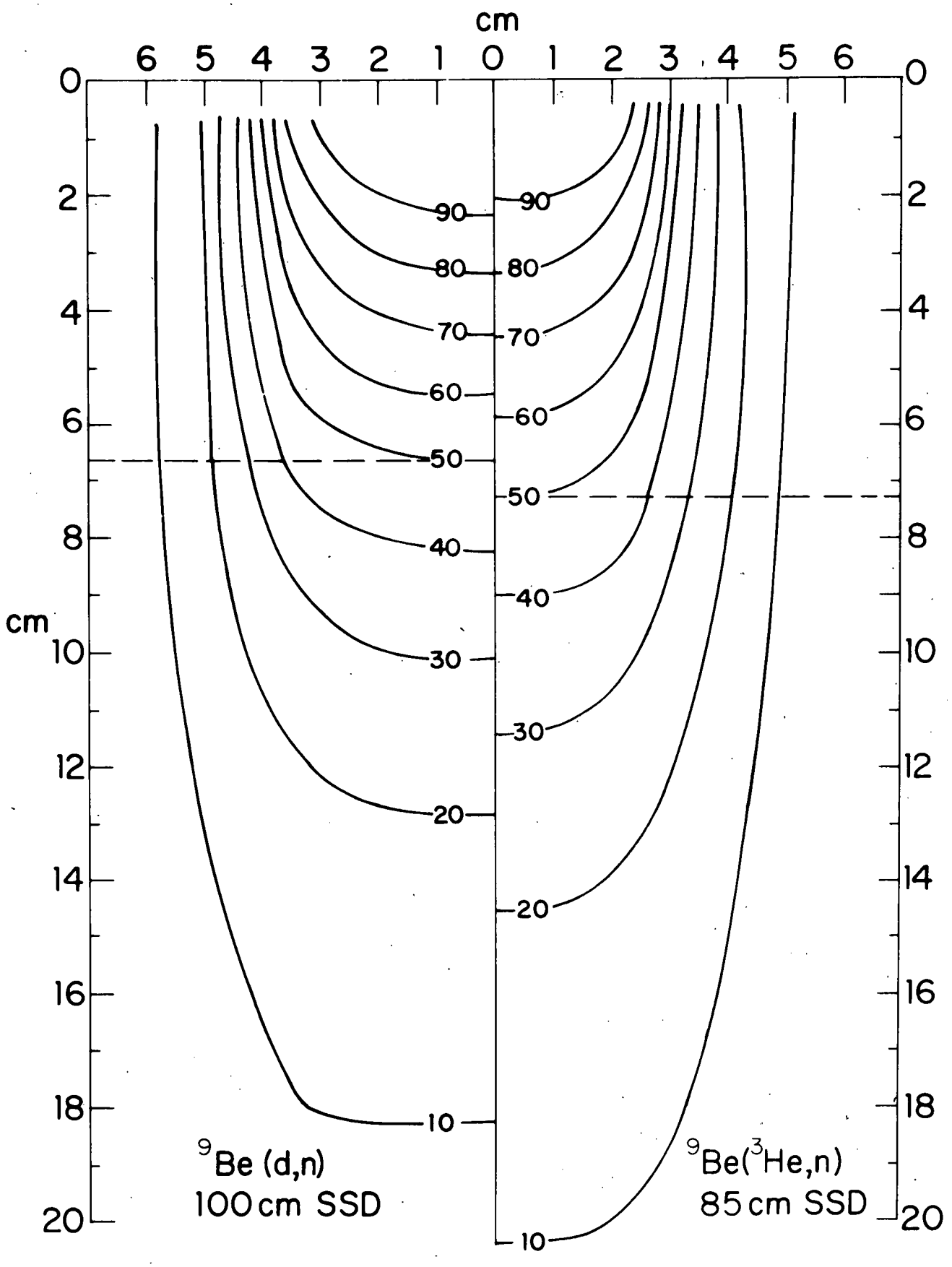

Figure 14. Iso-dose distributions for the ^{9}Be(^{3}He,n) and ^{9}Be(d,n) reactions.

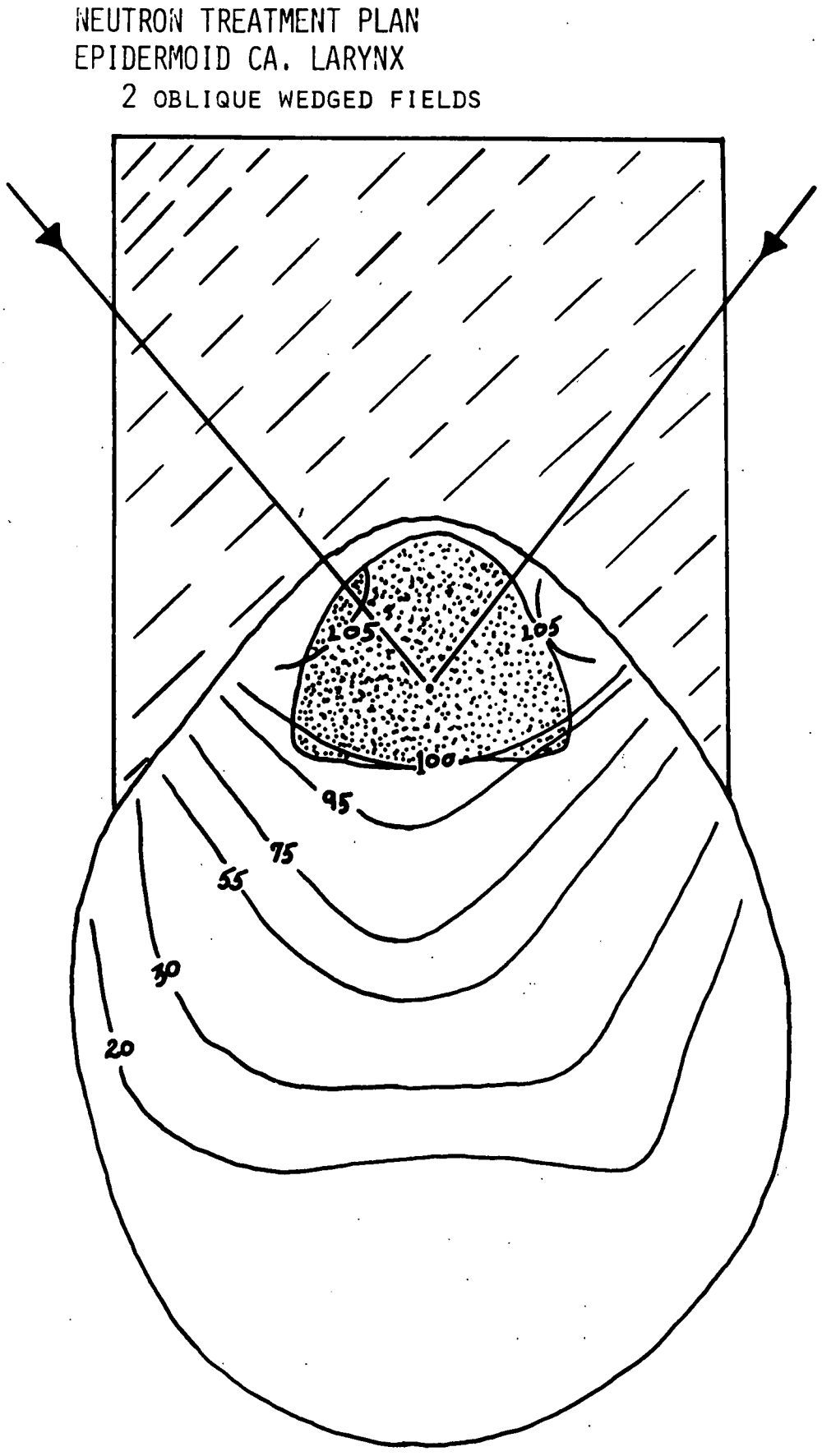

Figure 15. Neutron treatment plan for epidermoid carcinoma of the larynx.

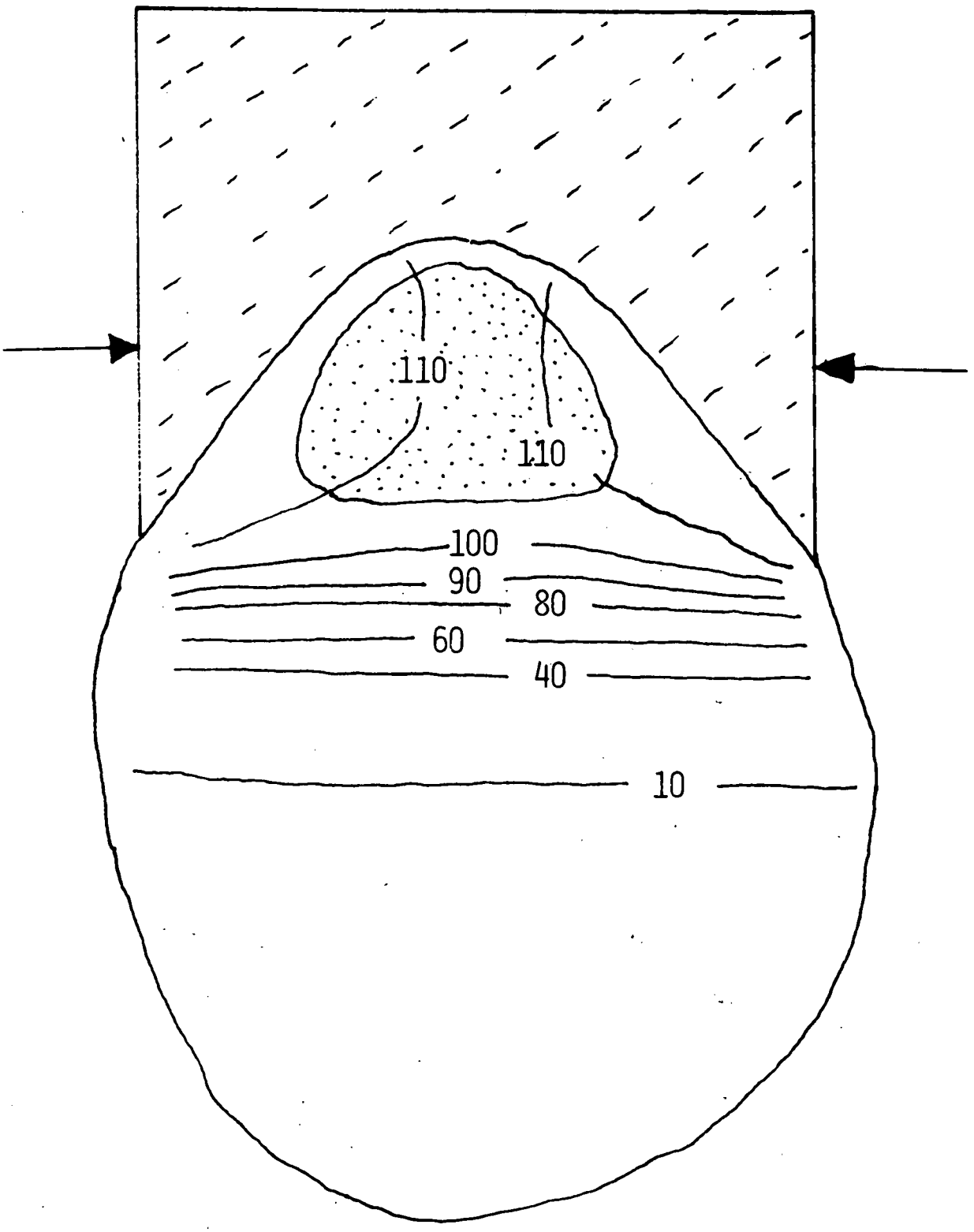

Figure 16. Neutron treatment plan for epidermoid carcinoma of the larynx using parallel-opposed bolused fields.

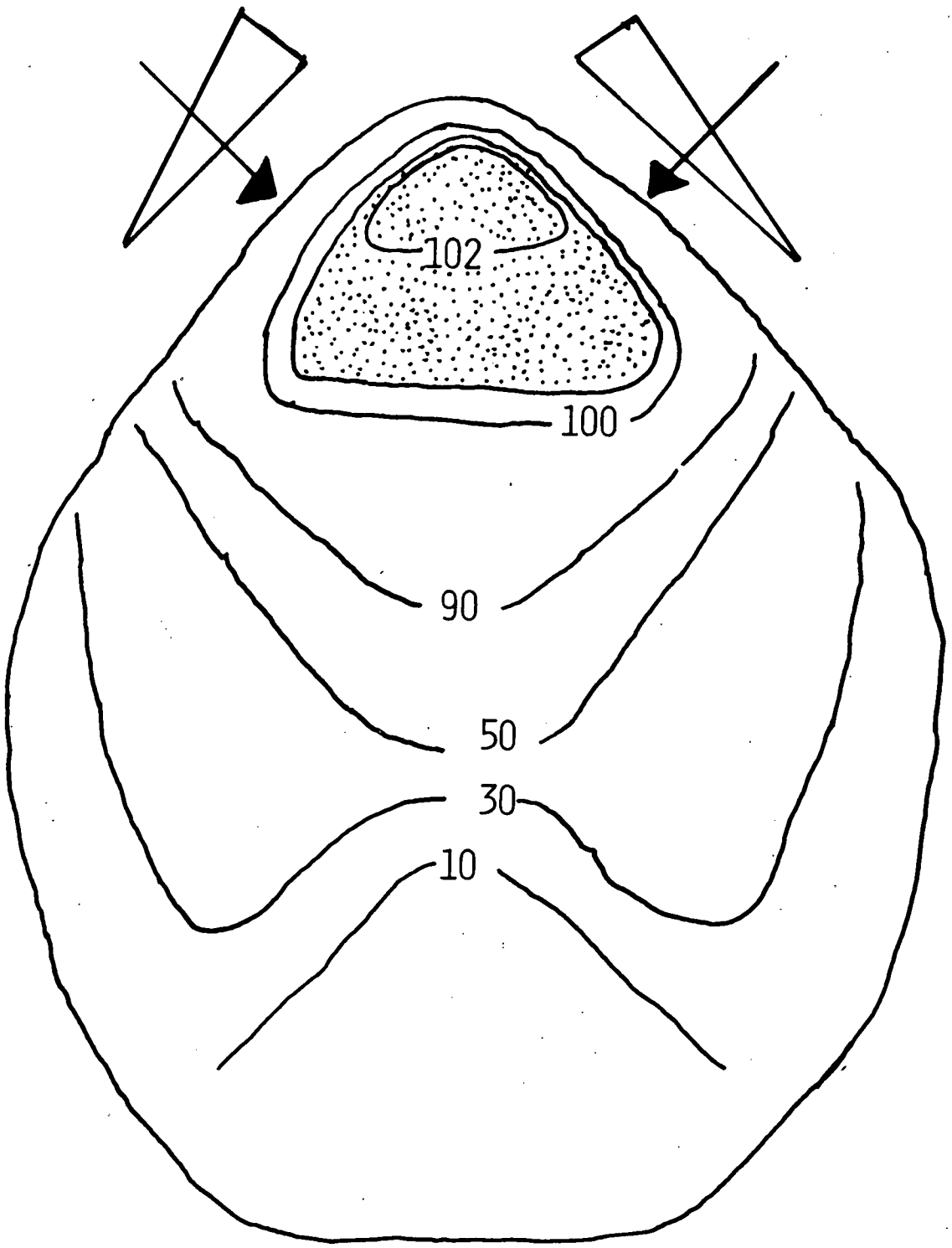

Figure 17. ^{60}Co Treatment plan for epidermoid carcinoma of the larynx.

densely ionizing resulting in LET values of greater than 200 keV/μ. Any variation of the neutron energy spectrum will alter this complex distribution of dose in LET and result in a change in the biological response.

To determine the degree of variation, dose distributions in LET have been measured at various positions within a water phantom for the collimated fields described above. Event spectra were measured with the T.E., 1.27 cm diameter, spherical proportional counter. Because the range of event sizes exceeds the dynamic range of the multichannel analyzer, it was necessary to obtain the data at three different gain settings. The data were reduced by a computer program which combined the spectra and smoothed the resultant spectrum, using a cubic spline technique.

Figure 18a shows the distribution of dose in LET, D(L), times the LET, L, as a function of L, for the ^{3}He induced field at a depth of 2.2 cm. This plot shows the various features, namely, the dose arising from the heavy recoils, the alpha particles, the low energy protons and the increasingly energetic protons. Figure 18b shows another way of presenting these data. E(L) is the portion of the dose which appears above a given value of LET.

Figure 19 shows how the major part of these distributions vary as a function of position within the field. The solid and dashed curves were obtained on axis, at depths of approximately 2 and 12 cm. There is observed, in both reactions, an increase in the portion of the dose delivered at lower values of LET as the depth is increased. That is, the average energy of the recoil protons increases with depth. This is consistent with the hardening of the neutron energy distribution observed with the activation foils. The dotted curves were obtained 2 cm inside the penumbra of the collimator. The neutron energy has been markedly degraded resulting in the recoil proton dose appearing at higher values of LET.

Figure 20 compares the E(L) distributions obtained for the two reactions at one depth. The ^{3}He induced field has a larger portion of its dose resulting from alphas and heavier recoils and the dose arising from the recoil protons is shifted to lower values of LET. Both effects are results of the higher average neutron energy of the ^{3}He induced field.

In order to estimate the variation of the biological response which would be associated with the measured distributions of dose in LET, and the increasing gamma dose at depth, the R.B.E. versus LET mammalian cell data of Barendsen et al. (7) were used to calculate R.B.E. values at a 0.5% survival level. These were

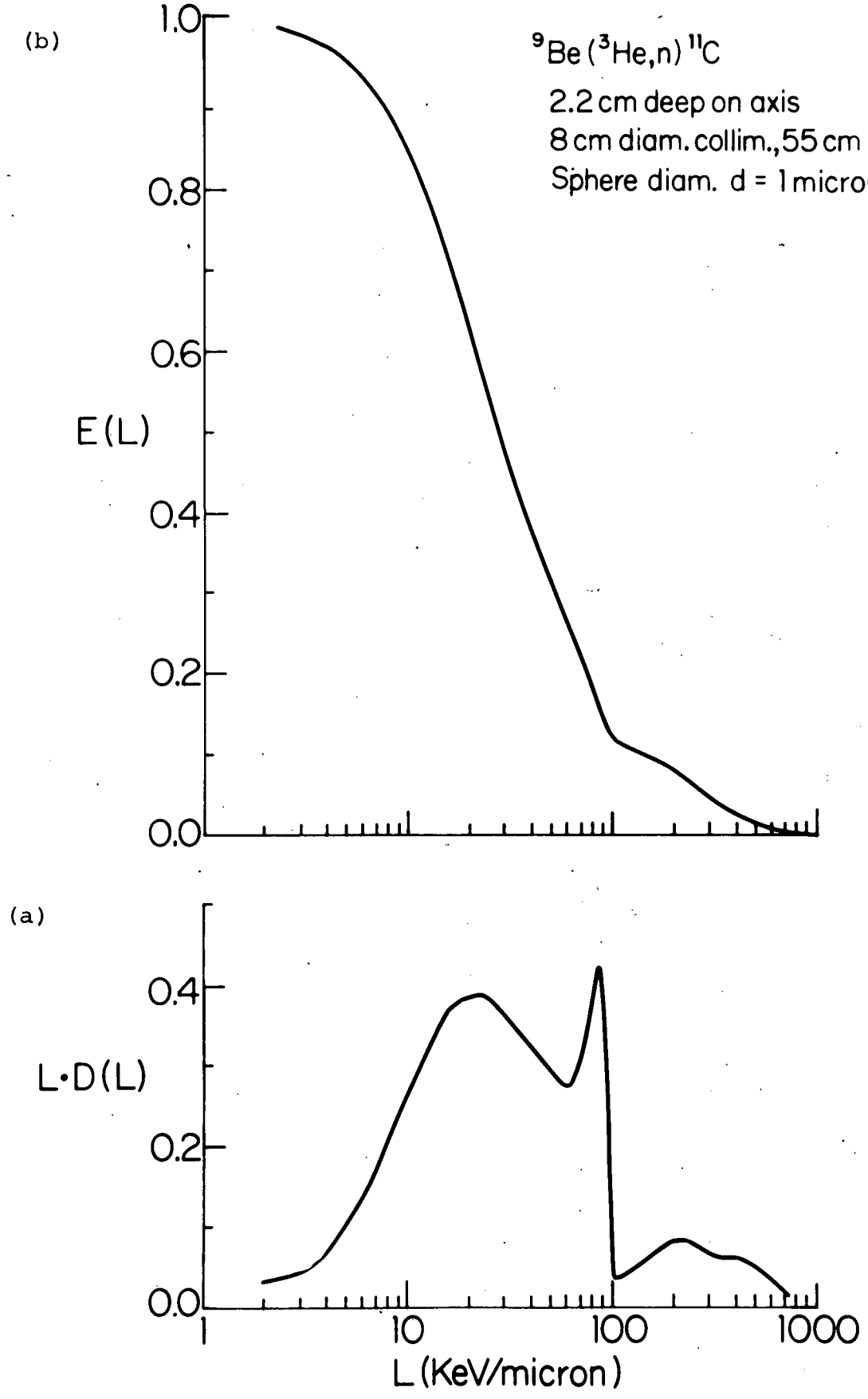

Figure 18. (a) Distribution of dose in LET, D(L) times the LET (L) vs LET for $^{9}Be(^{3}He,n)$ reaction.
(b) E(L), the portion of dose appearing above a given value of LET for the above reaction.

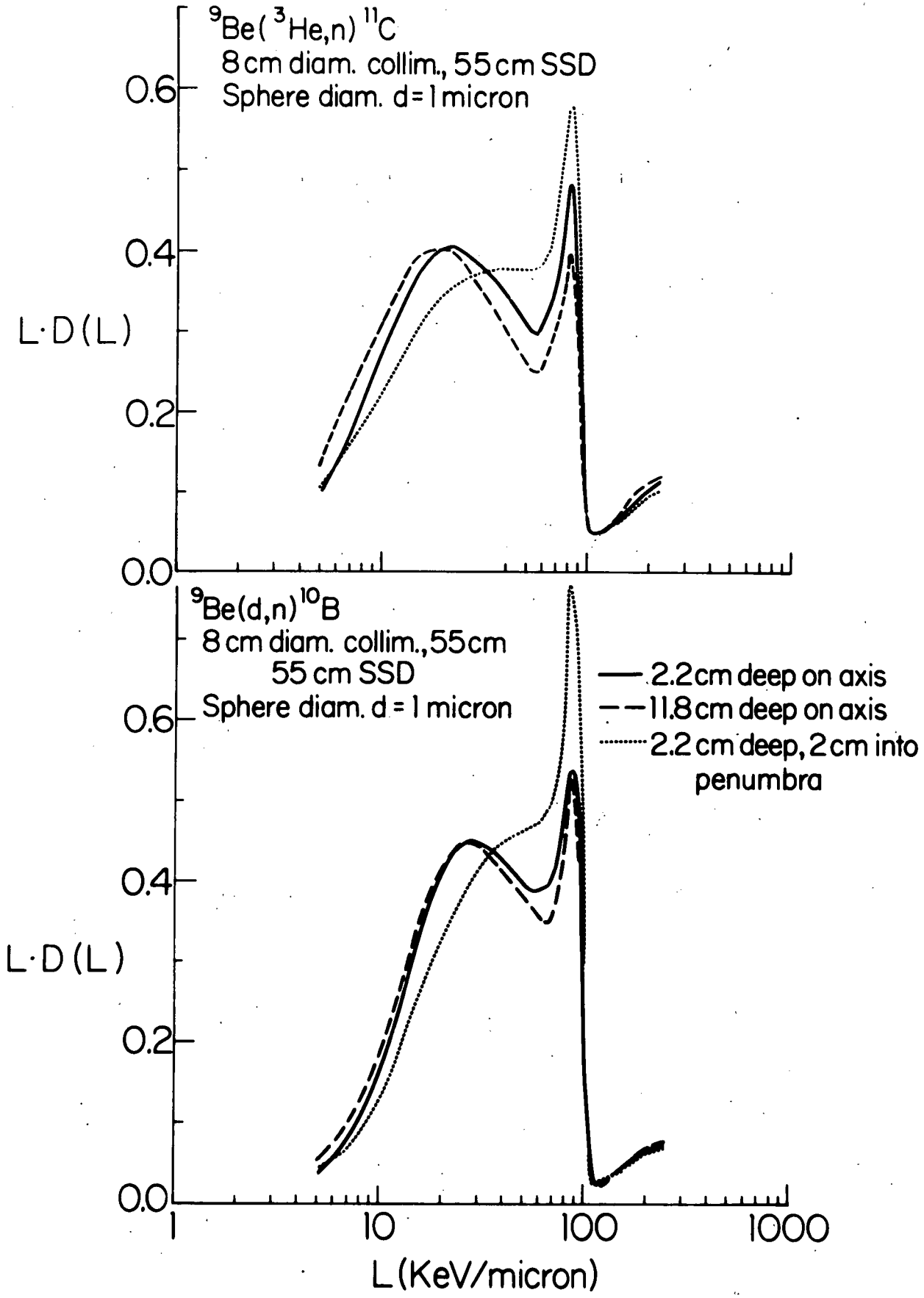

Figure 19. LET distributions for two neutron producting reactions as a function of position in the neutron field.

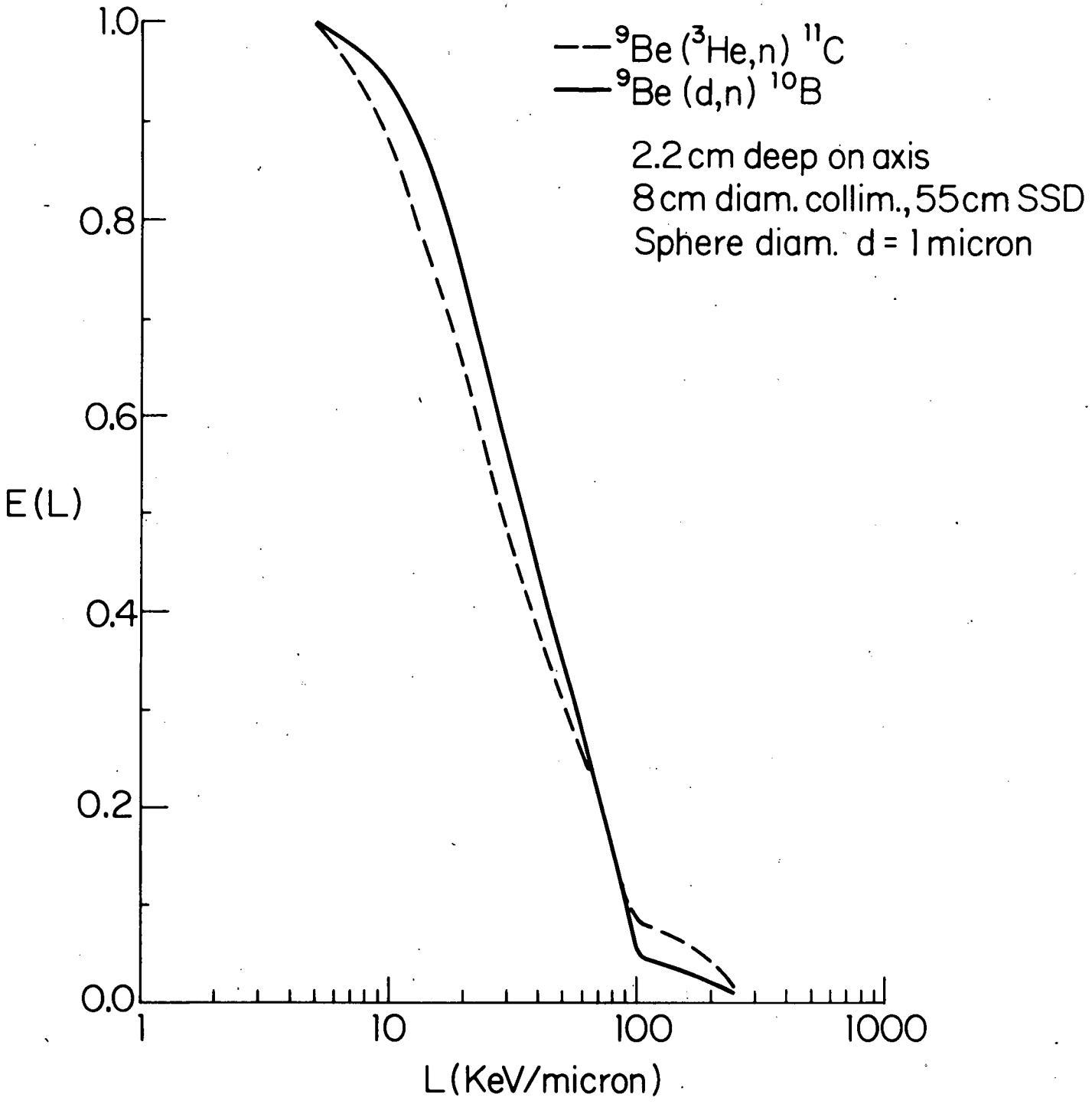

Figure 20. E(L) distributions for two neutron producing reactions measured on axis at a depth of 2.2 cm in water.

then compared with the HeLa S-3 cell survival curves measured at three depths, for both the Be+d and Be+^{3}He fields. These measurements were made in collaboration with B. Djordjevic.

At a 0.5% level of survival the R.B.E. approaches the ratio of D_o values obtained for the neutron and X-ray survival curves. Using an X-ray D_o value of 119±8 rads gives a range of predicted D_o values shown in Figure 21. These show that little variation of biological response is expected with depth. Experimental D_o values, shown as data points, are consistent with this. They lie somewhat below the calculated values, but considering the accuracy of the calculation, the agreement is reasonable.

Finally, we conclude, on the basis of the results presented here, that the physical properties of these fast neutron fields are such that compact cyclotrons must be considered as strong candidates for wide spread fast neutron radiotheraputic sources.

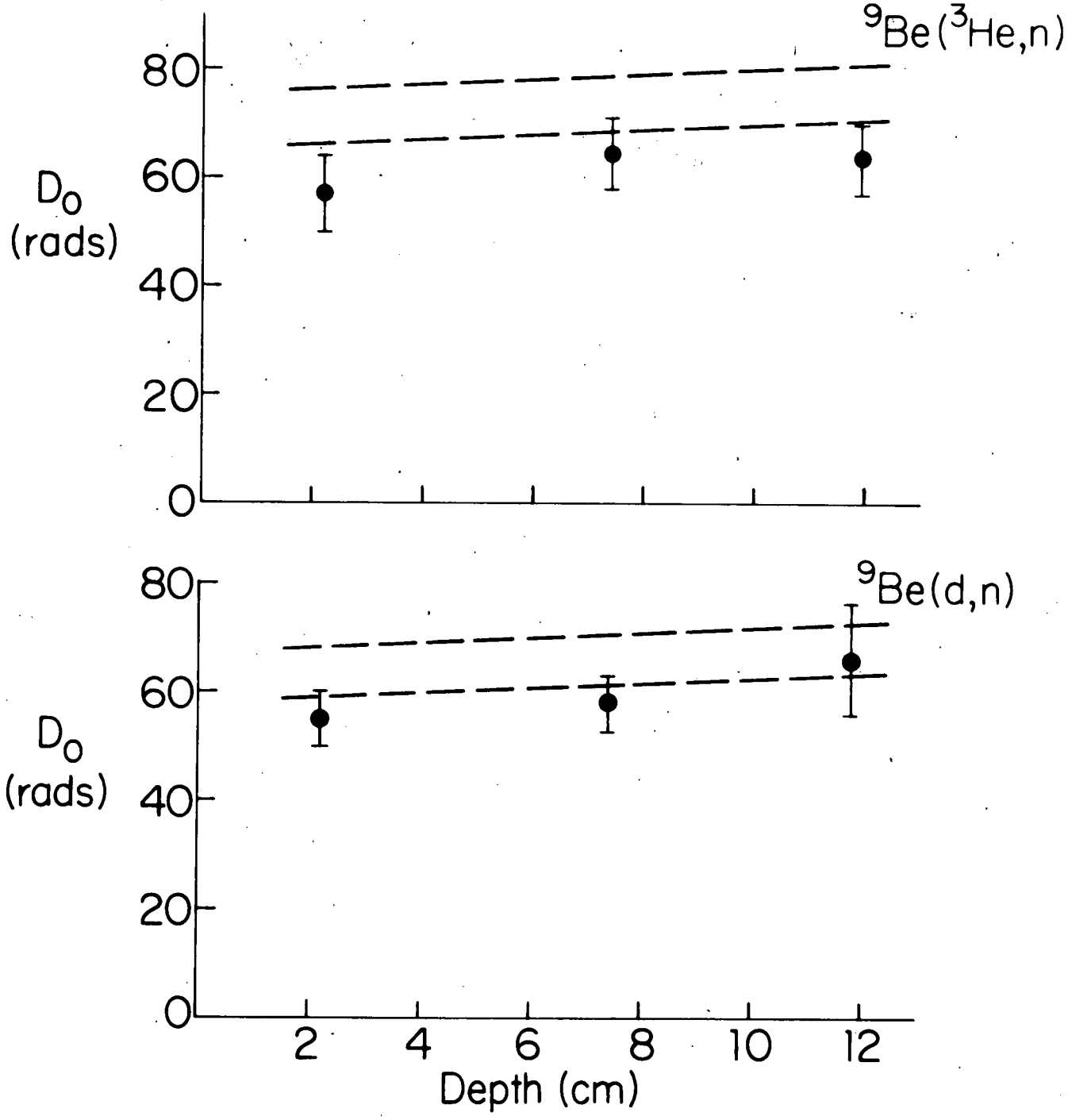

Figure 21. Comparison of calculated and measured D_o values for HeLa cells at three depths in water.

III. CONSTRUCTION AND TESTING OF A TISSUE EQUIVALENT ABSORBED DOSE CALORIMETER FOR FAST NEUTRONS

(T.R. Canada, J.C. McDonald, A. Mittleman and J.S. Laughlin)

A. Introduction

The tissue equivalent calorimetric dosimeter system has been designed to provide a primary calibration standard for the ionization chambers and other secondary dosimetric systems used to measure fast neutron dose. All major parts of the calorimeter have been constructed of Shonka A-150 plastic. The dimensions of the central absorber are identical with the collecting volume of the tissue equivalent ionization chamber shown in Figure 2B.

The principal of quasi-adiabatic calorimetry (21) relies on accurate determination of the time-temperature behavior of the central absorber and its surrounding adiabatic jacket. The environment surrounding the absorber and jacket is maintained at a constant temperature by a massive control shield which is regulated by an electronic temperature controller. During electrical calibration or irradiation, both the absorber and jacket are heated at the same rate so that the temperature difference between them, and thus the heat loss from the absorber, is small. Measurement of temperature drift rates before and after calibration or irradiation and the temperature rise during energy input yields the net rate of temperature change due to energy absorption.

B. Experimental Apparatus

Since the basis of calorimetric dosimetry is to measure all of the energy imparted to the central absorber by the radiation field, it is necessary to reduce heat losses to a minimum. Conductive losses are minimized by supporting internal components with hollow nylon screws which provide approximate point contact. Convective heat loss is minimized by evacuating the calorimeter to approximately 1 millitorr. The primary means of energy flow out of the central absorber is through radiation. This effect was reduced by the coating of all internal surfaces with gold to reduce emissivity.

The calorimeter is shown in Figure 22 attached to a portable vacuum pumping system and placed in a 50 x 50 x 50 cm polystyrene tank. The tank is normally filled with water which is heated to approximately 5° above room temperature by a circulating thermal regulator. The water bath is maintained at the desired temperature to within $\pm 0.02^{\circ}C$. Further isolation

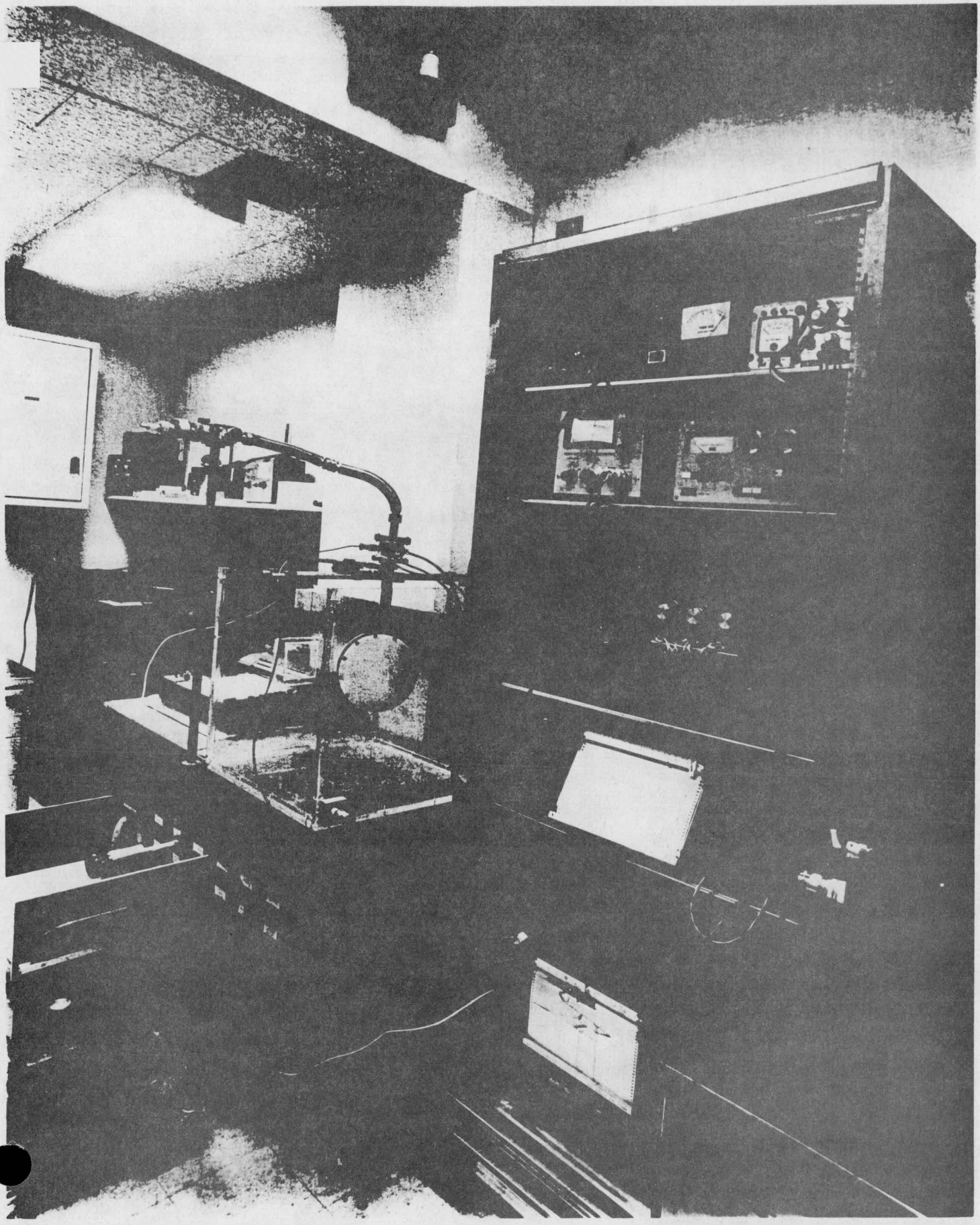

Figure 22. Tissue equivalent calorimeter in polystyrene water tank. Electronics rack housing Artronix temperature regulator, Wheatstone bridges and recorders.

is designed into the calorimeter (Figure 23). The temperature of the outermost element, the control shield, (Figure 23) is maintained to within ±1 x 10^{-3}°C/hr. by an Artronix temperature regulator. This unit delivers an amount of power to the shield (by ohmic heating of the plastic itself) which is proportional to the resistance of a thermistor placed in the shield. Buffer shields placed between the adiabatic jacket central absorber assembly and the control shield isolated the inner units from short term temperature changes at the shield.

Thermistors and heating leads are attached to the adiabatic jacket and central core. The resistances of the thermistors are measured by Wheatstone bridge circuits which are monitored by Keithley 150 electrometers. The outputs from these electrometers are recorded on a dual input, strip chart recorder which provides an equivalent temperature versus time record. Temperature stability of 1-5 x 10^{-6}°C/min for periods of an hour have been obtained at the central core. A calibration circuit like that of ref. 8 is used to heat the central core and the adiabatic shield at equal rates. The heating is done using the internal resistance of the Shonka plastic.

C. Results and Discussion

The temperature response of the central core, observed when the calorimeter was exposed to ∿1200 rads of 300 kVp X-rays, is shown in Figure 24A. For this trial exposure, a high level of thermal stability was not necessary. Stabilities of at least a factor of ten better than that shown here are routinely achieved.

Figure 24B compares the central core response when the core alone and both the core and the adiabatic jacket are electrically heated. The "after-heating" stability is clearly superior when both units are heated to the same temperature. These curves, however, show the characteristics of non-uniform heating of the core. The lack of linearity during the heating and the overshoot after the power has been turned off indicates that the wafer is not only being heated uniformly because of its inherent electrical resistance but that "hot spots" are also developing.

To determine the source of this problem studies have been made of the resistance properties of the Shonka A-150 plastic, by measuring the resistance of various lengths of the plastic (all having a cross sectional area of 4 cm^2). Good electrical contact with the plastic was difficult to achieve. The contact resistance was minimized when Electrodag 451* was sprayed onto the desired

*Obtained from Acheson Colloids, Port Huron, Michigan.

surfaces. The results showed a resistivity of 53.6 ohm-cm and a contact resistance of 26 ohms. The resistivity has previously been (9) estimated to be approximately 50 k ohm-cm. Our results indicate that they may not have adequately accounted for the contact resistance. On the basis of these results the internal and surface resistances of the calorimeter's central core are estimated to be approximately 3.4 and 56 ohms, respectively. It is this large surface resistance which gives rise to the non-uniform heating distribution. Work is presently underway to determine a method to reduce this contact resistance to a negligible level. Alternate methods of delivering heat to the various units are also being studied.

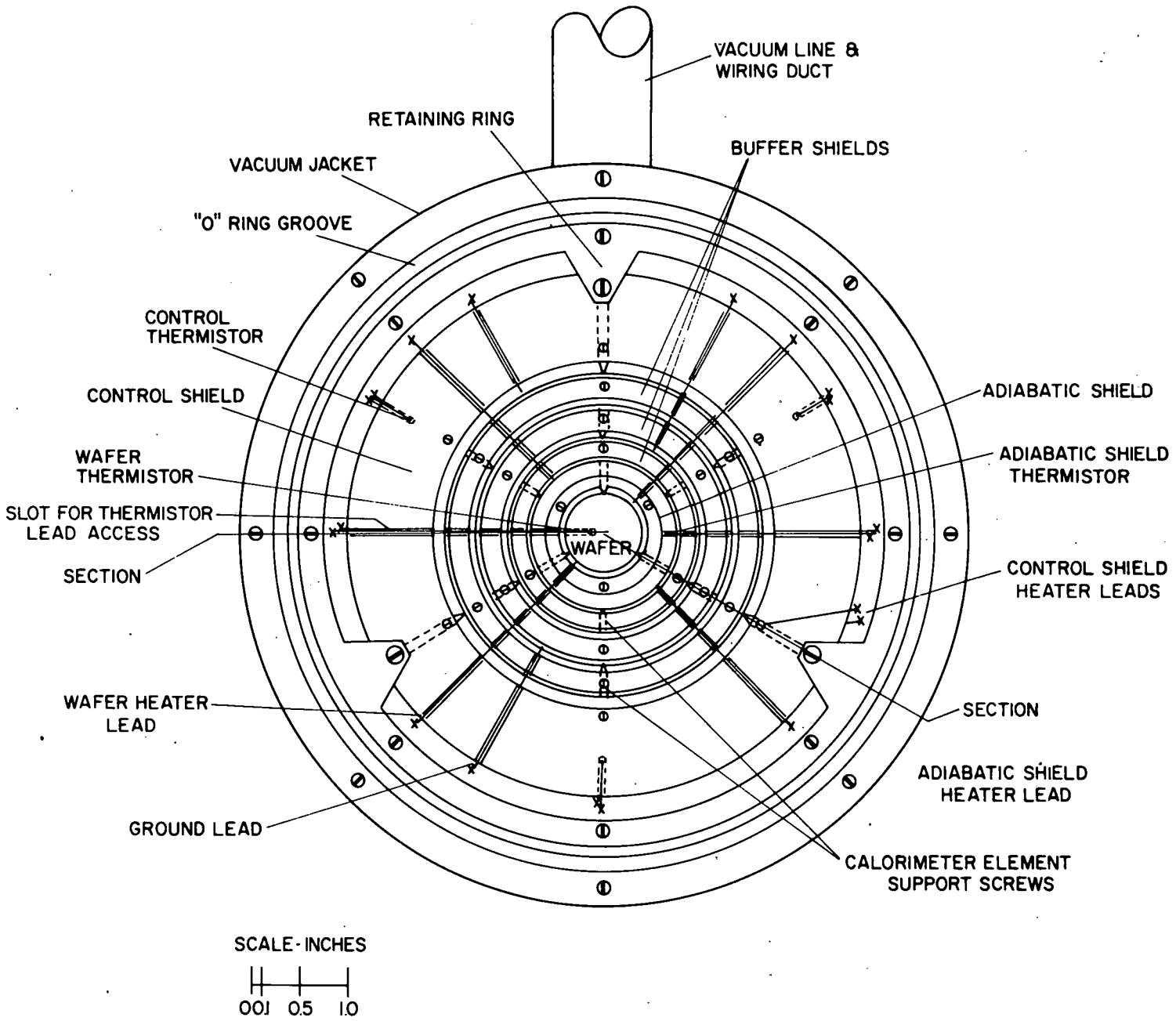

Figure 23. Interior construction of tissue equivalent calorimeter, all major components are Shonka A-150 T.E. plastic.

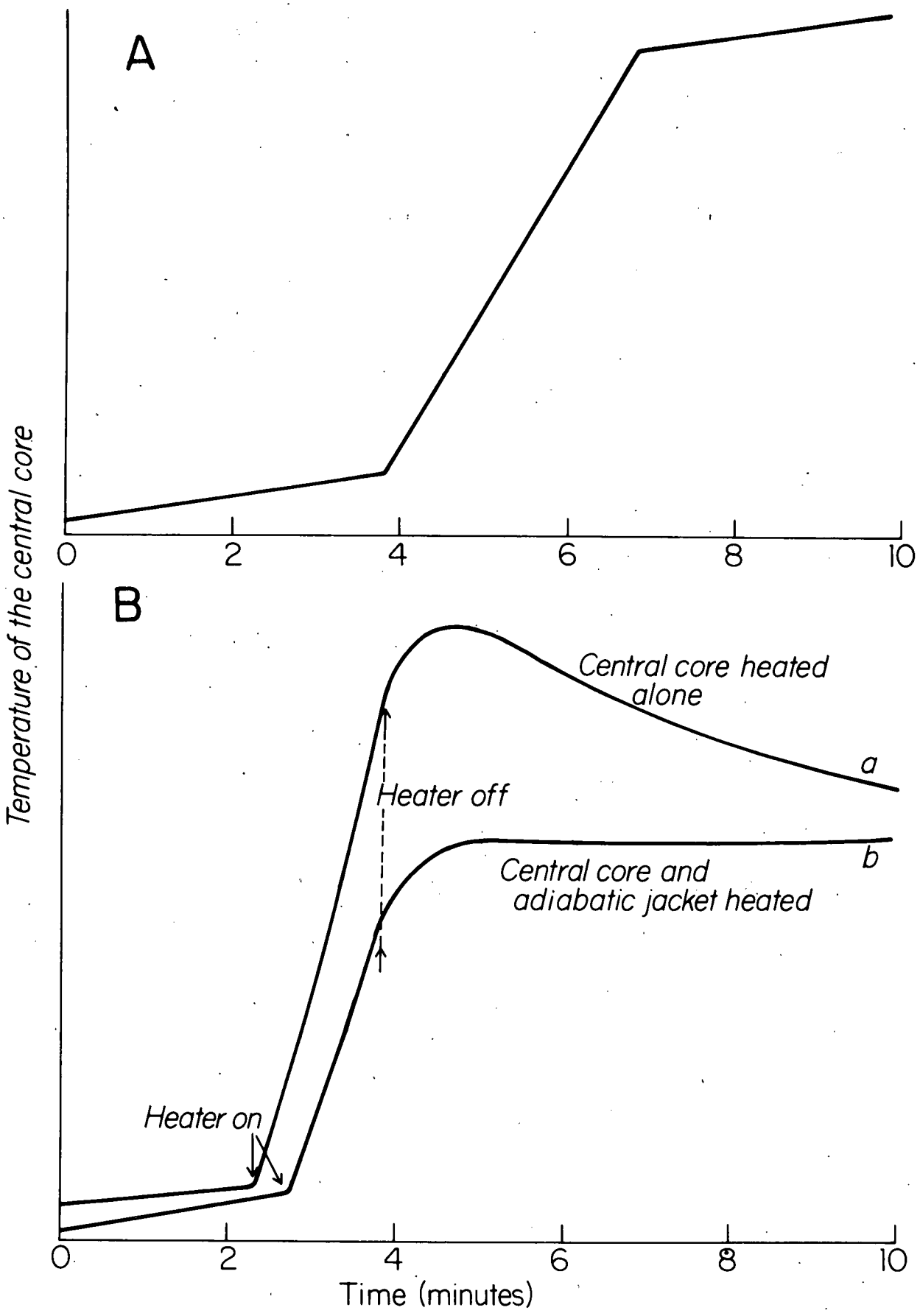

Figure 24. Temperature response of calorimeter central core. (a) Irradiation with ≈1200 rads 300 kVp x-rays (b) Electrical calibration of core alone and core plus adiabatic jacket.

IV. DOSIMETRY FOR ^{252}Cf MEDICAL NEUTRON SOURCES
(L.L. Anderson)

The Memorial Sloan-Kettering Cancer Center is participating in the U.S. Atomic Energy Commission's program to evaluate ^{252}Cf neutron sources for radiation therapy. Dosimetry projects during the year have included the preparation of a survey report on ^{252}Cf neutron and gamma ray dosimetry, extensive ion chamber measurements of neutron and gamma ray dose distributions in tissue-equivalent fluid, and a preliminary evaluation of an apparent problem with high beta ray dose rates from singly-encapsulated, stainless steel afterloading cells.

The status of dosimetry for ^{252}Cf medical neutron sources has been thoroughly treated in a report (10) on an intercomparison study performed here for an advisory committee to the Division of Biology and Medicine. This report contains an analysis of data from four sets of measurements and five sets of calculations performed at various laboratories to assess neutron and gamma ray dose distributions for application to brachytherapy. Among effects investigated for the purpose of explaining discrepancies in the data were (1) source size and encapsulation, (2) phantom size and material, including air interface effects, (3) energy response and material of detector, and (4) neutron spectrum assumptions. The results of this study were presented in part at the Third International Conference on Medical Physics, July 30-August 4, 1972 in Goteborg, Sweden (11) and have been submitted for publication.

Both neutron and gamma ray absorbed dose distributions have been measured in the vicinity of ^{252}Cf applicator tube sources. These measurements employ paired miniature ionization chambers having tissue-equivalent wall and gas for total neutron-plus-gamma ray dose, and aluminum walls and argon gas for gamma ray dose only. In order to obtain high ion current, without sacrificing spatial resolution by increasing chamber volume, six ^{252}Cf sources are suspended simultaneously at equivalent geometrical positions in radial fashion about the chamber. A multiple-source manipulator apparatus designed specifically for this purpose permits positioning at 0.5 cm intervals up to 8.5 cm in both radial and axial directions. Data analysis is not yet complete, but the results show agreement to within about 10% with values recommended in the intercomparison report and with previous measurements here in nylon phantom (12).

The results of RBE and OER measurements last year using HeLa cells have been published (13). This paper includes a derivation of formulas for correcting measured RBE and OER values to those which would be expected for the ^{252}Cf neutron component only.

The neutron OER formula is at variance with a previously published formula (14) derived in another laboratory, but the error in the latter case has been acknowledged (15).

In a collaborative study with E. Hahn (22) a series of rabbit testes irradiations with ^{252}Cf sources has been performed, using the exposure apparatus developed last year, in studies designed to measure the RBE of ^{252}Cf neutrons with respect to ^{60}Co and ^{226}Ra gamma rays. Reduced sperm production in the post-irradiation period serves to indicate the extent of radiation injury to the spermatogonial cell system. Semen samples are collected weekly and the concentration, motility and number of abnormalities are determined. Preliminary data indicate that 50 rad and 100 rad ^{252}Cf neutrons produce similar response curves. More data are required.

The singly encapsulated, stainless steel afterloading cells recently made available by the Atomic Energy Commission for ^{252}Cf brachytherapy have dimensions (6 mm length and 0.5 mm diameter) which make them quite compatible with the narrow lumens and sharp bends of after loading tubing in a typical removable implant. However, it is apparent that the very thin encapsulation also permits a large fraction of the emitted beta radiation to penetrate the wall. Before the new sources can be applied clinically, it is essential that the contribution of beta rays to the total dose be accurately determined.

Preliminary measurements have been made, using thermoluminescent dosimetry, of the combined beta and gamma ray dose rate at 0.5 cm from a source of this type, along the transverse axis. The 0.5 cm distance is important clinically since sources in actual implants will be spaced about 1 cm apart. The measurements were made in a polystyrene phantom, using ^{7}LiF powder (99.99% ^{7}Li) placed in a ring-shaped cavity in the plane perpendicular to the source axis and passing through its center. Without added filtration the combined β-γ absorbed dose rate from a source of 0.5 μg nominal activity was found to be 19 $\pm$1 rad/h. Further measurements employed close-fitting cylindrical gold and platinum filters of various thickness. For a platinum filter of wall thickness 0.23 mm, the β-γ dose rate was reduced to a 4.5 rad/h, roughly twice the dose rate expected (on the basis of measurements with much thicker filters) from gamma rays alone. The corresponding neutron dose rate, 4.7 rad/h, produces negligible interference with the ^{7}LiF measurement.

V. GERMANIUM GAMMA CAMERA
(J.F. Detko and J.S. Laughlin)

A. Introduction

The solid state detector program is currently centered upon the development of a semiconductor gamma camera from an array of ultra pure germanium diodes and the evaluation of the utility of this device in both clinical and biological applications. Demonstration of the practical imaging capabilities of a small prototype germanium camera has been presented in previously reported biological tests on small mammalian organs (16,17). For convenience of reference these results are illustrated in Figure (25). The lower half of the figure is a germanium camera image of a rat thyroid obtained after the animal's injection with ^{123}I(159 keV). The upper section of the figure is an anterior and posterior photograph of the thyroid taken following its excision. The individual thyroid lobes are resolved in the gamma camera image although their separation is less than 4 mm. Ultra pure germanium diodes have been chosen over lithium drifted diodes in this work because of their superior bulk and surface properties and because they do not require the lithium drift process and continuous cryogenic cooling. The camera development is based upon an orthogonal strip detector geometry developed in this program for such use and tested originally in a silicon lithium drifted diode (18,19). The orthogonal strip geometry is shown in Figure (26)a with its mode of signal address schematically depicted in (b) of the same figure.

B. Prototype Germanium Camera

1. Image resolution compared to scintillation camera. In the previous report (16) initial electrical and biological test results were presented for a prototype gamma camera with a (2 x 2)cm^2 detector. This consisted of a 36 cell matrix of 5mm thickness which was shown to have a spatial resolution of less than 4mm from both phantom and point source measurements. The successful operational testing of this prototype device provided a basis for construction of a larger matrix which will be discussed below. Figure (27) was obtained with the (2 x 2)cm^2 prototype matrix and is a photograph of a storage scope image of a ^{99m}Tc phantom which appeared in the last report. The image of the same phantom obtained with an Anger scintillation camera through the same collimator is shown in Figure (28). The separate radioactive regions in the phantom could not be resolved by the Anger camera under optimum operating conditions. A similar test was made with a ^{99m}Tc point source and showed the

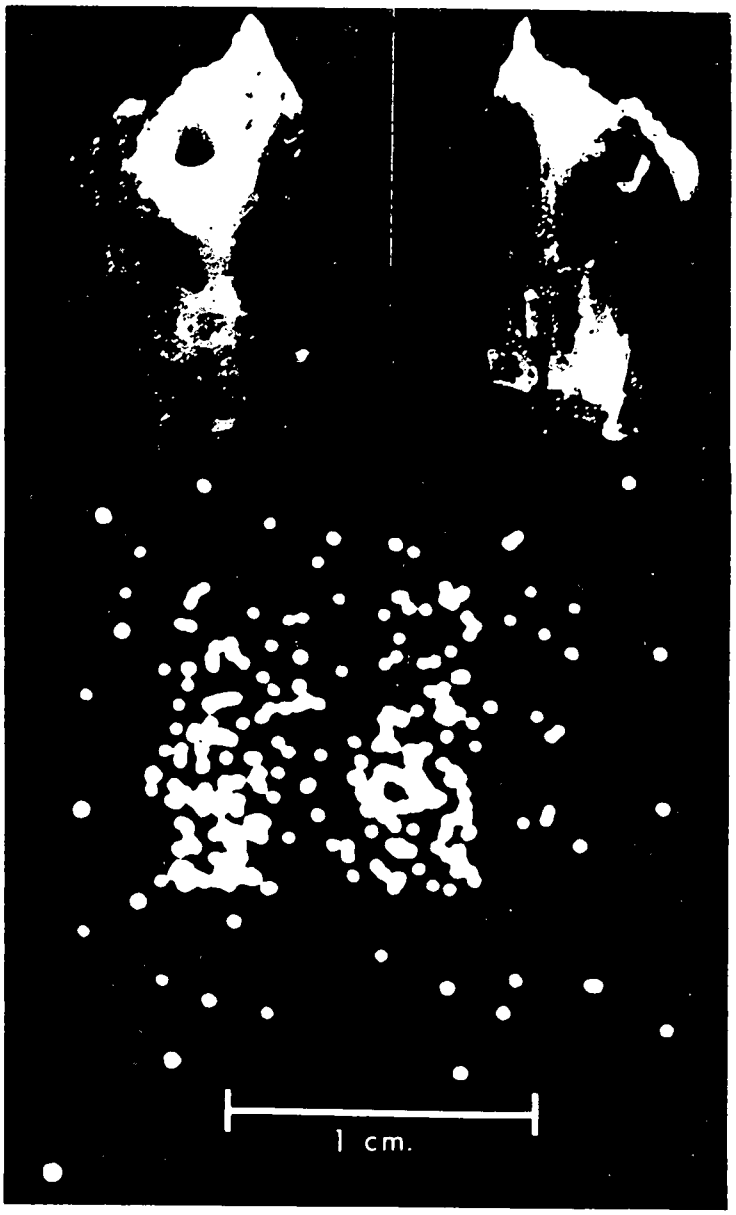

Dot image of thyroid of rat injected with ^{123}I

Figure 25. A. Anterior and posterior photograph of excised rat thyroid
B. Germanium camera image of rat thyroid after animal was injected with ^{123}I (159 KeV).

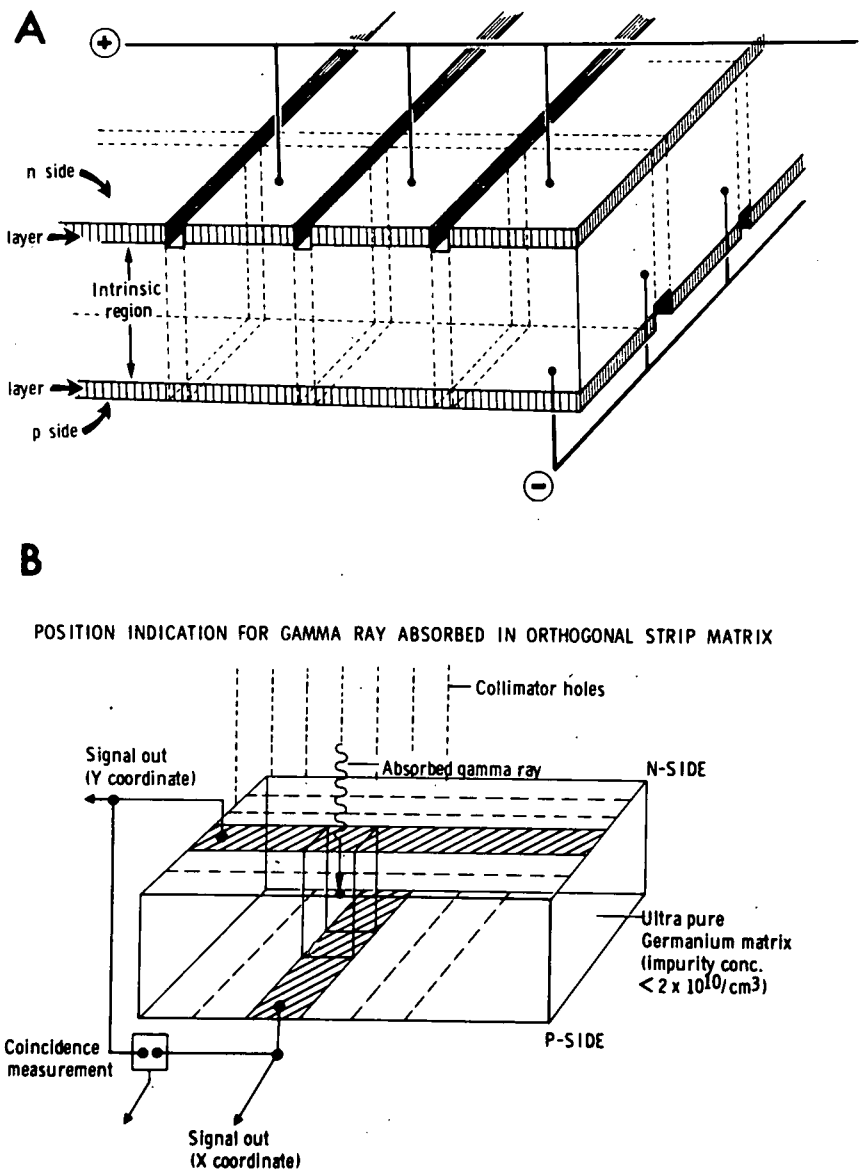

Figure 26. A. Orthogonal Strip Geometry
B. Mode of Signal Address

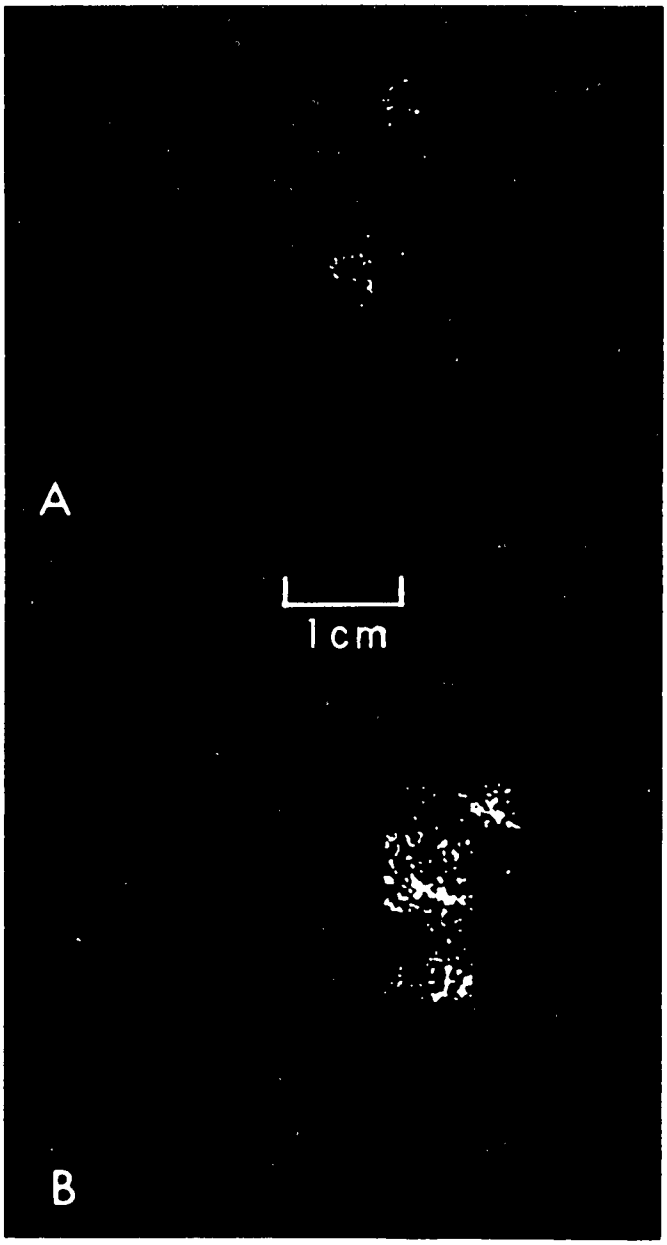

Figure 27. A. Image of ^{99m}Tc (140 KeV) phantom containing 3 and 4 mm diameter hot spots, 9 mm separation
B. 5 mm hot spot has been introduced between the other two

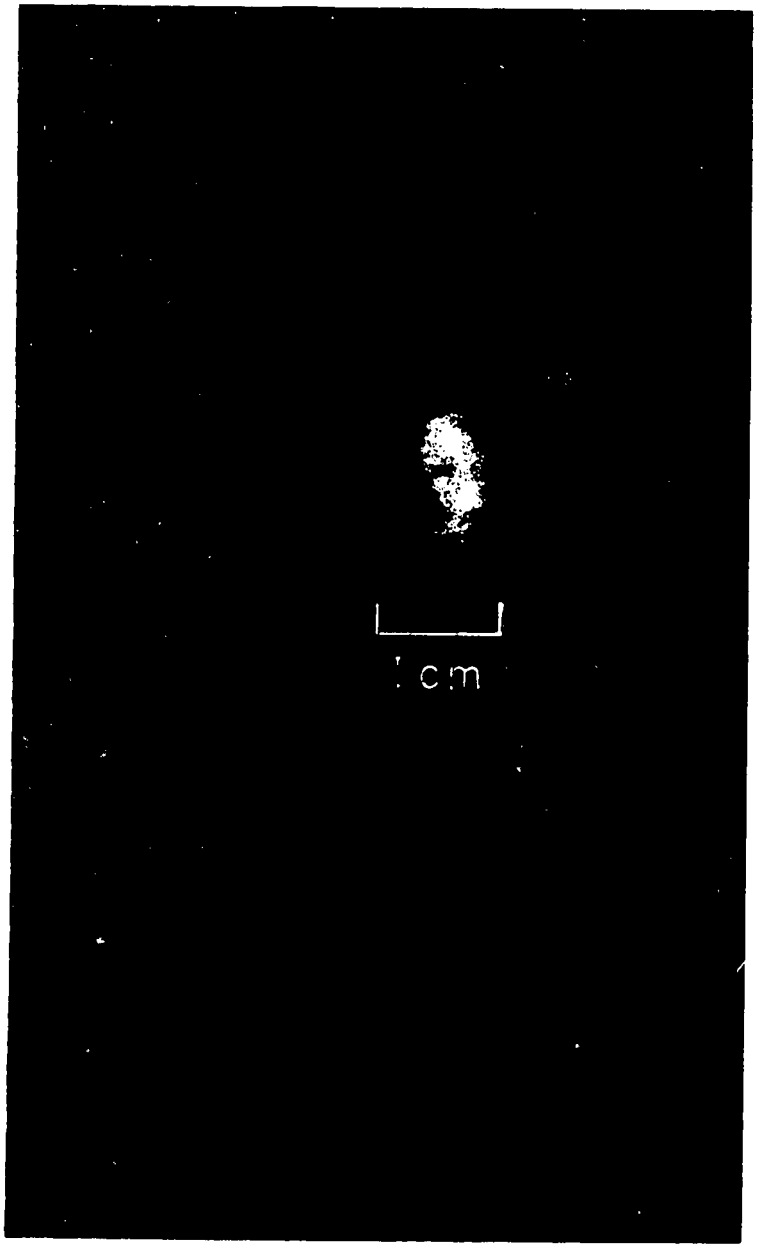

Figure 28. Anger scintillation camera image of ^{99m}Tc phantom through the same collimator used with the germanium camera. The separate hot spots are not resolved.

inability of this instrument to detect position separations of less than one centimeter at this isotope energy.

2. Electrical tests. The previous report contained plotted data of the variation of interelectrode strip groove resistance with reverse bias across the matrix. The importance of adequate groove resistance, as noted there, is in the effective elimination of "crosstalk" between electrode strips and in the reduction of charge loss at the electrode strip boundaries through the restriction of the electric field lines to the electrode strip regions. Following the previous report period further tests were conducted on the prototype matrix. The importance of adequate groove resistance levels is further demonstrated by the data appearing in Figure (29) where measured noise levels (FWHM) for the p-side electrode strips have been plotted against reverse bias across the matrix. The upper half contains the noise levels (FWHM) for each p-side electrode strip as obtained with an r.m.s. volt meter. In the lower half, the same data were derived directly from measurements of a ^{57}Co(122 keV) source. The agreement between the two sets of data is quite good considering that the ^{57}Co measurements reflect other sources of line broadening over and above those it has in common with the rms measurements. It can be seen in this figure that for both sets of data, the resolution curves become relatively flat over a range of between 180-220 volts reverse bias. This is the voltage range at which the depletion region reaches the bottom of all p-side grooves for the prototype device. The noise contribution due to diode capacitance, which varies with reverse bias, is insignificant in these resolution curves. This is evidenced in the lower half of the same figure by the early flattening of the plot of the measured resolution for a representative n-side strip. The relatively narrow voltage range in which these curves level out for all p-side electrode strips is a coarse but significant indication of a corresponding uniformity of crystal impurity concentration along the grooves. These data imply, at most, a variation of 22% in impurity concentration along the equally spaced grooves.

3. Stability tests. The question of matrix stability was further pursued with the first prototype matrix. The device was temperature cycled several times between liquid nitrogen and room temperature without opening the cryostat. The total exposure time to room temperature was two days. No degradation in spectral resolution was observed. Following a single opening of the cryostat to room ambient conditions, measurements with ^{57}Co were repeated. Initially these showed that some broadening of the base of the 122 keV ^{57}Co peak on the low energy had resulted for two p-side electrodes while the resolution (FWHM) remained unchanged. These

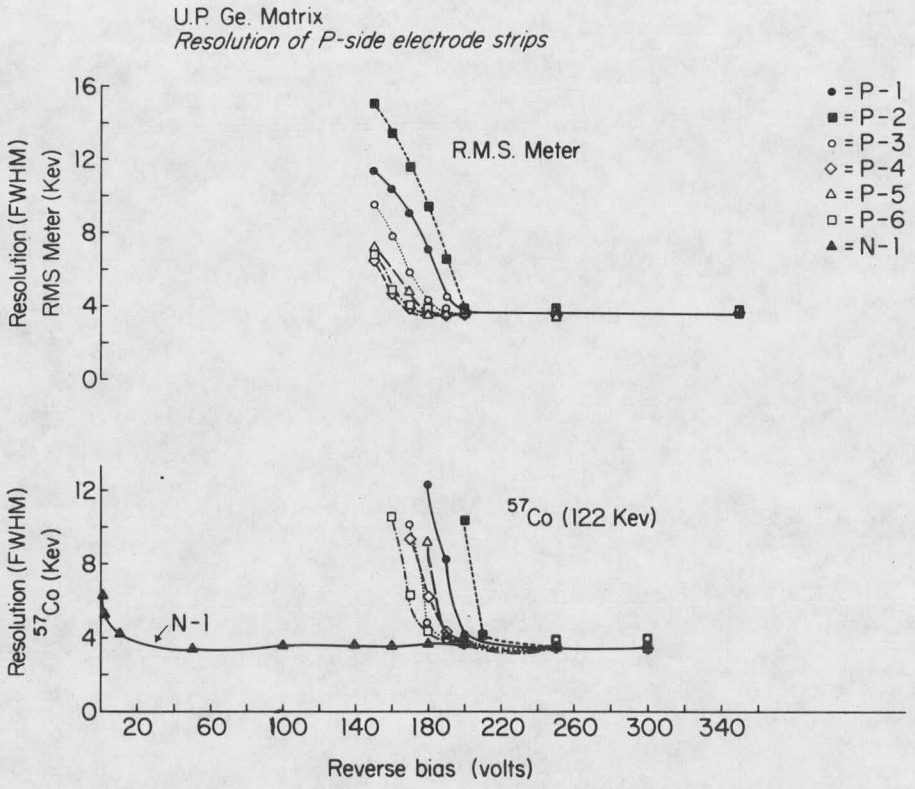

Figure 29. Resolution of p side electrode strips versus reverse bias

conditions became somewhat worse with time and eventually appeared at all p-side strips. The deterioration was the result of matrix surface contamination occurring during opening of the matrix to air.

C. Construction and Testing of Ultra-Pure Germanium Diodes

1. Diode 2038-4. The facilities for producing boron implanted p^+ contacts, which were the type selected for the orthogonal strip matrix arrays of the gamma camera, were assembled at the end of the last report period. This apparatus is modelled, in principal, after that used at General Electric where this type of p^+ contact was developed.* The first ultra pure germanium wafer employed with these facilities was a p type (4 x 4)cm, 4.4mm thick wafer with a specified impurity concentration of 2.1×10^{10} atoms/cc. This was supplied as a research specimen by the vendor prior to delivery of two 5 cm diameter pieces on order for purchase.

Repeated efforts were made to produce an acceptable diode from this germanium sample using the new boron implant facilities and the conventional techniques for forming a lithium diffused n^+ layer. However the resolution of the ^{57}Co(122 keV) peak never improved below 6 keV even when the bias across the diode was well beyond the depletion voltage. Further, probing the diode surface with a ^{57}Co(122 keV) pencil beam showed that the diode had regions of charge trapping where the 122 keV and 136 keV peak were barely discernible in the pulse height spectrum. Further work with this germanium was suspended and work begun on a smaller diameter (3 cm) wafer of ultra pure germanium from crystal #415 to determine whether the poor diode quality achieved with the previous piece was due to the germanium or to an inferior p^+ boron contact.

2. Diode 415-5. The same procedures were followed in the construction of a diode from the new material and yielded a diode with resolution (FWHM) of under 4 keV for .5 microsecond filter time constants and a warm f.e.t. The overvoltage capability of the diode was almost twice as great as the depletion voltage before breakdown. These results, while not dramatic, demonstrated the effectiveness of the boron contact applied with the "in house" facilities and provided a basis for attempting to construct diodes from the then received larger diameter (5 cm) wafers of ultra pure germanium from crystal #2077. The two sections of this p-type crystal were of 5 and 10mm thickness before processing.

3. Diode 2077-5. It was decided to attempt construction

*General Electric Co., Schenectady, N.Y.

of a diode from the thinner piece first. The quoted impurity concentration for this section was 1.6 x 10^{10} atoms/cc. This was cut into an approximate 12 cm^2 square. The same fabrication procedures were employed as with #415. A diode of acceptable quality was obtained. In the reprocessing which required repeated etching of the wafer, the thickness was reduced to 4mm. Spectral measurements of ^{57}Co were made on this diode with a room temperature f.e.t. and yielded resolution of 3.5 keV. Considering the rather high capacitance (around 45pf) of the nearly 12 cm^2 diode this resolution figure contains a substantial electronic component which when eliminated yields a resolution of less than 3 keV. Measurements of diode capacitance versus reverse bias were made with the diode in its cryostat at liquid nitrogen temperatures. According to the vendor's quoted impurity concentration for the germanium, the voltage expected to produce full depletion of the diode was 144 volts. The capacitance measurements indicated that full depletion occurred below 100 volts as can be seen from curve A in Figure (30). This data implies an impurity concentration of less than 1 x 10^{10} atoms/cc. Since this diode was considered a suitable candidate for eventual conversion into an orthogonal strip matrix, it was removed from its cryostat for the additional processing which has been found necessary to protect the electrodes. Further spectral measurements were made following this which showed that the overall resolution (FWHM) had improved to below 3 keV for ^{57}Co(122 keV) even with a warm f.e.t. Elimination of the room temperature electronic noise component reduced the resolution figure to around 2 keV. Capacitance measurements were repeated and are shown as curve B of Figure (30). The flattening of the curve at under 100 volts again implies an impurity concentration of less than 1 x 10^{10} atoms/cc. The capacitance of 45pf measured at depletion of the diode was around 6% higher than the calculated geometric capacity. This is not an unusual discrepancy.

As a check on the impurity concentration inferred from the capacitance measurements with the capacitance bridge, a collimated source of ^{241}Am(59 keV) was used to measure the variation in the thickness of undepleted germanium with bias voltage at different points on the diode surface. Particular attention was given to the use of short filter time constants in the amplifier in these measurements to minimize the effects of charge diffusion into the depletion region as observed by Baertsch (20). The capacitance variation with reverse bias calculated from these absorption measurements is shown in Figure (31) along with the capacitance bridge measurements for ready comparison. It can be seen that the radiation attenuation measurements also support a value of less than 1 x 10^{10} atoms/cc for the impurity concentration of the ultra pure germanium. A plausible reason for the discrepancy

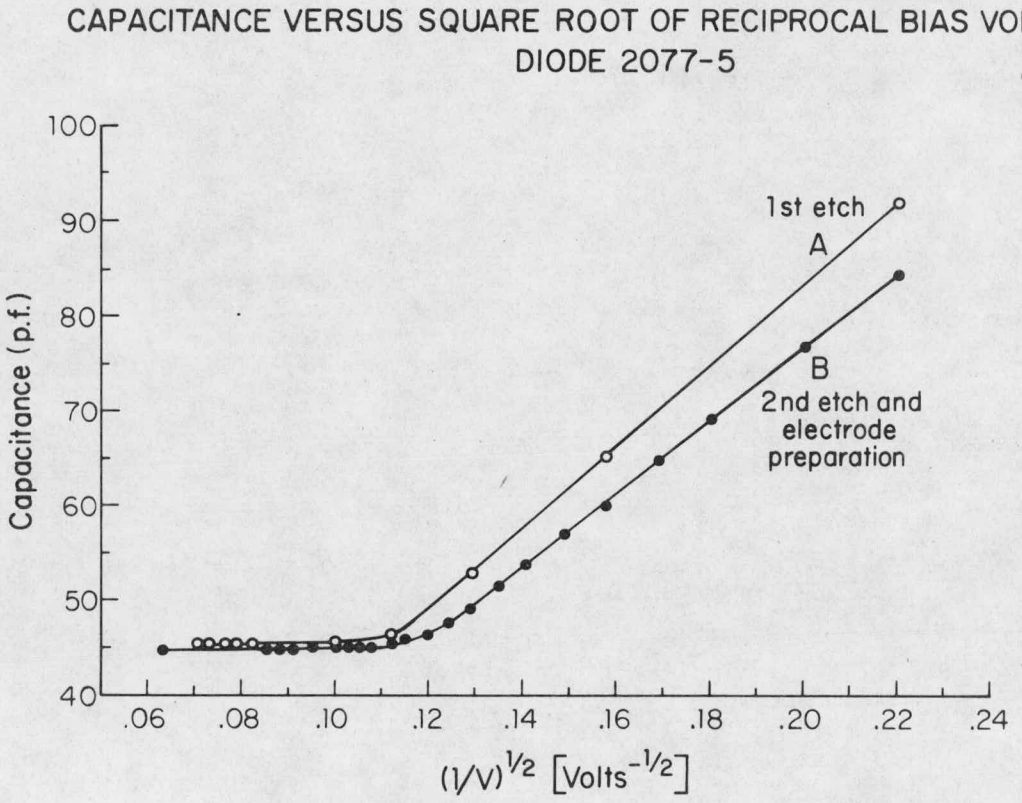

Figure 30. Diode 2077-5. Capacitance versus reverse bias measured with capacitance bridge.

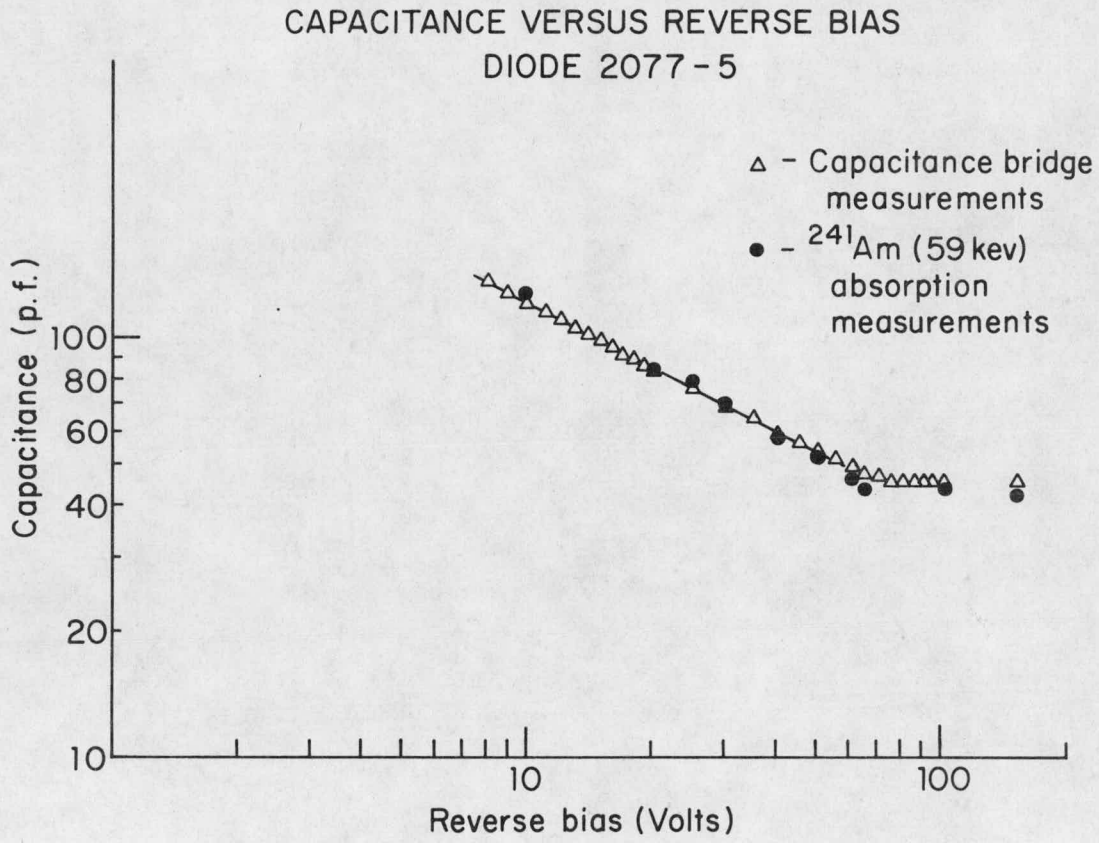

Figure 31. Diode 2077-5. Capacitance versus reverse bias determined by ^{241}Am(59 KeV) absorption measurements.

between these data and the vendor's figure for impurity concentration is that the germanium in the diode under test came from the more central region of the original wafer since the latter was cut into a square. A higher impurity concentration in the outer section of the germanium wafer could have contributed undue weight to the value of impurity concentration obtained for the total volume.

4. Diode 2077-9. The second section of crystal 2077 was nearly 10mm thick upon receipt. The specified impurity concentration was $.8 \times 10^{10}$ atoms/cc. A diode was fabricated from this material using the same procedures employed with the first section from the same crystal. The diode electrodes were prepared in advance for eventual matrix formation since there was no longer reason to doubt the effectiveness of the boron implant procedures. As before, a square piece of germanium was cut from the original wafer after lapping both of its faces into within .0005 inch of plane parallelism. The finished diode, after etching, had dimensions of 12 cm^2 x 8.7mm in thickness. Spectral measurements of ^{57}Co(122 keV) were made and a resolution of 2.5 keV was obtained with the room temperature f.e.t. A typical spectrum obtained on the multichannel analyser is shown in Figure (32). Capacitance measurements were made to determine the variation of depletion thickness with bias voltage. The measured capacitance of 19.41pf at 250 volts, which is essentially the depletion voltage, is remarkably close to the value obtained for the calculated geometric capacitance of 19.43pf. The occurrence of full depletion of the diode at 250 volts or less implied an impurity concentration of $.6 \times 10^{10}$ atoms/cc as compared to the manufacturers specification of $.8 \times 10^{10}$ atoms/cc. Since the performance of this diode was better than the one produced from the thinner section of the crystal and since it offered a greater gamma ray absorption efficiency with its more than twice greater thickness, it was decided to form the first of the larger matrix arrays from this diode. To confirm the results of the capacitance measurements with the bridge and to obtain an appreciation of the degree of uniformity of the impurity concentration across the diode, radiation attenuation measurements were again made with a narrow beam probe constructed from a collimated source of ^{241}Am. The capacitance calculated from typical data obtained from these measurements and its variation with depletion voltage is shown in Figure (33). Capacitance values obtained with a capacitance bridge are shown in the same figure. The agreement between the two data sets over the range of 20 to 200 volts is quite good, the extreme deviation between points being less than 8%. In an effort to detect small variations in the depletion voltage over the diode surface, a narrow beam probe was constructed from a collimated source of ^{125}I(28.4 keV). A germanium

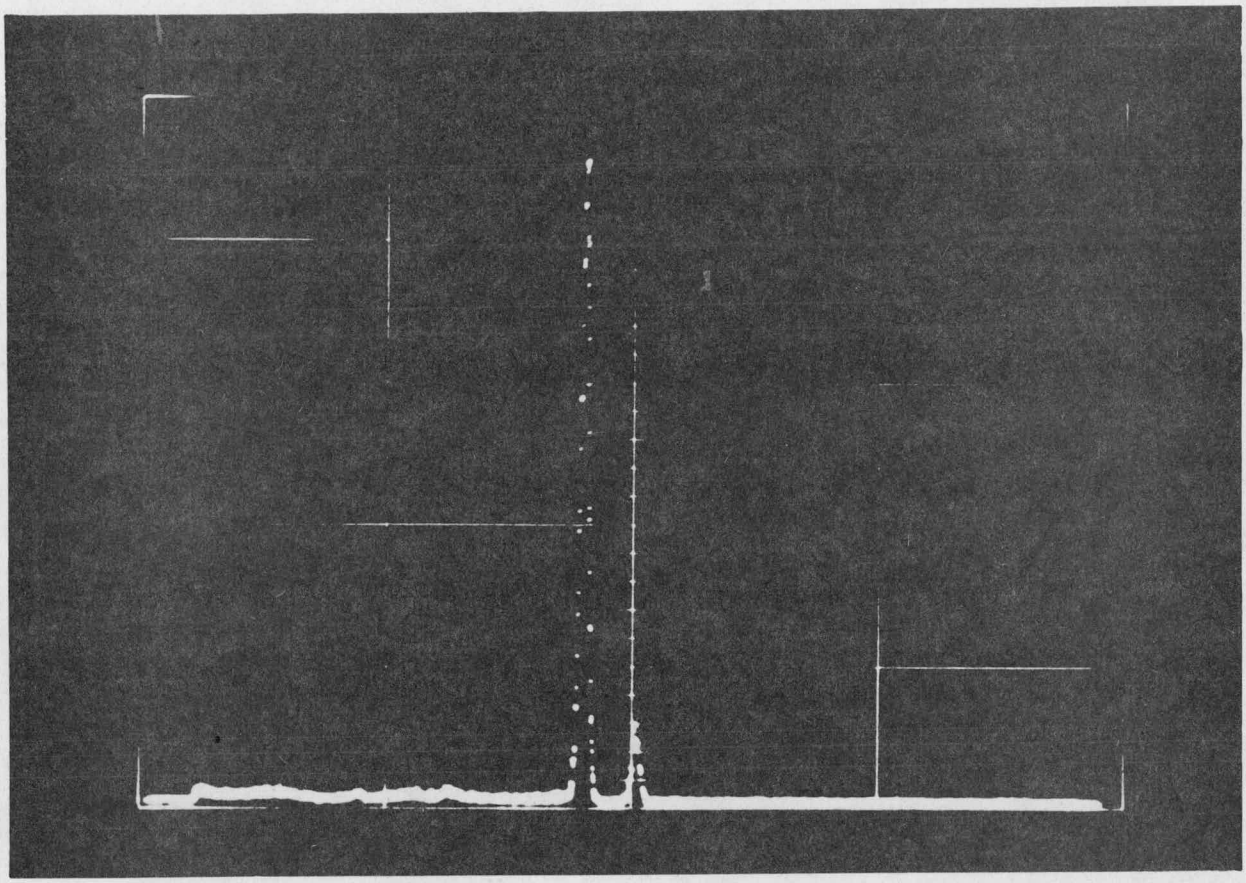

Figure 32. Typical spectral measurement of ^{57}Co (122 KeV) with diode 2077-9. Resolution of 122 KeV peak is 2.5 KeV (FWHM).

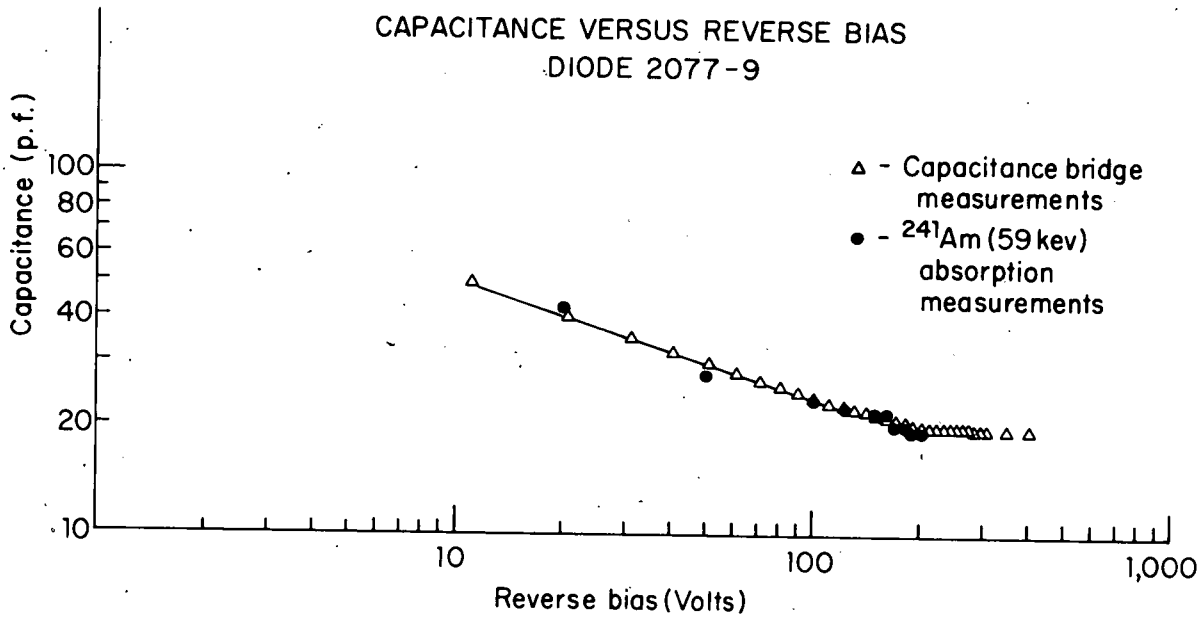

Figure 33. Diode 2077-9. Capacitance versus reverse bias from capacitance bridge and ^{241}Am(59KeV) absorption measurements.

layer of around .075mm is sufficient to attenuate a beam of this energy by 50%. It was expected that the full depletion voltages obtained from these measurements for the diode would be somewhat less than the full value because of the diffusion of charge carriers from the undepleted region on the p-side into the depletion region. However no slow charge component peak associated with this effect could be observed on the multi-channel analyzer. The absorption measurements with ^{125}I at .25 microsecond filter time constants indicated that the voltage for full depletion is between 210 to 220 volts. This is consistent with the capacitance bridge measurements and the radiation absorption measurements obtained with the ^{241}Am source of Figure (33) where capacitance curves depart from linearity at 200 volts.

To test the uniformity of the charge collection process in the diode before using it in the construction of a matrix, a 1mm beam of ^{57}Co(122 keV) gamma rays was used to probe the diode response at sample points on the diode surface. As part of this work an intensity profile measurement of the narrow beam source was made to determine the effective beam diameter at the diode surface. The axis of the collimated source was mounted at a right angle to the shaft of a micrometer and moved across the edge of a lead absorber in increments of .005 inch. The distance between the source aperture and the plane of the lead absorber was 1 cm. The radiation passing the edge of the source was monitored with the diode which was located immediately beneath. The thickness of the lead was such that the transmission was effectively zero (less than 10^{-7}) when the source aperture was over the lead slab. The data so obtained are presented in Figure (34). Each point represents the integration of the counts under the 122 keV photopeak at the particular source position. It can be seen that the intensity across the beam axis rises from 10% to 90% of its full intensity in about 1.2mm. Measurements were made of diode response to this source at twenty different points over the diode p-side surface. A resolution of 2.5-2.7 keV for the 122 keV photopeak was obtained at all positions with a warm f.e.t. while the charge collection efficiency varied less than 5% for the entire set of measurements.

The photoelectric absorption efficiency of the diode was measured relative to a one inch thick sodium iodide crystal for both ^{57}Co(122 keV, 136 keV) and ^{99m}Tc(140 keV). At these energies, this thickness of sodium iodide crystal provides 100% absorption efficiency. Such data provide a basis of comparison between the diode and the orthogonal strip matrix formed from the diode. For both isototpes, a collimated source was fixed in position and the detectors moved under them in turn. The ^{57}Co source

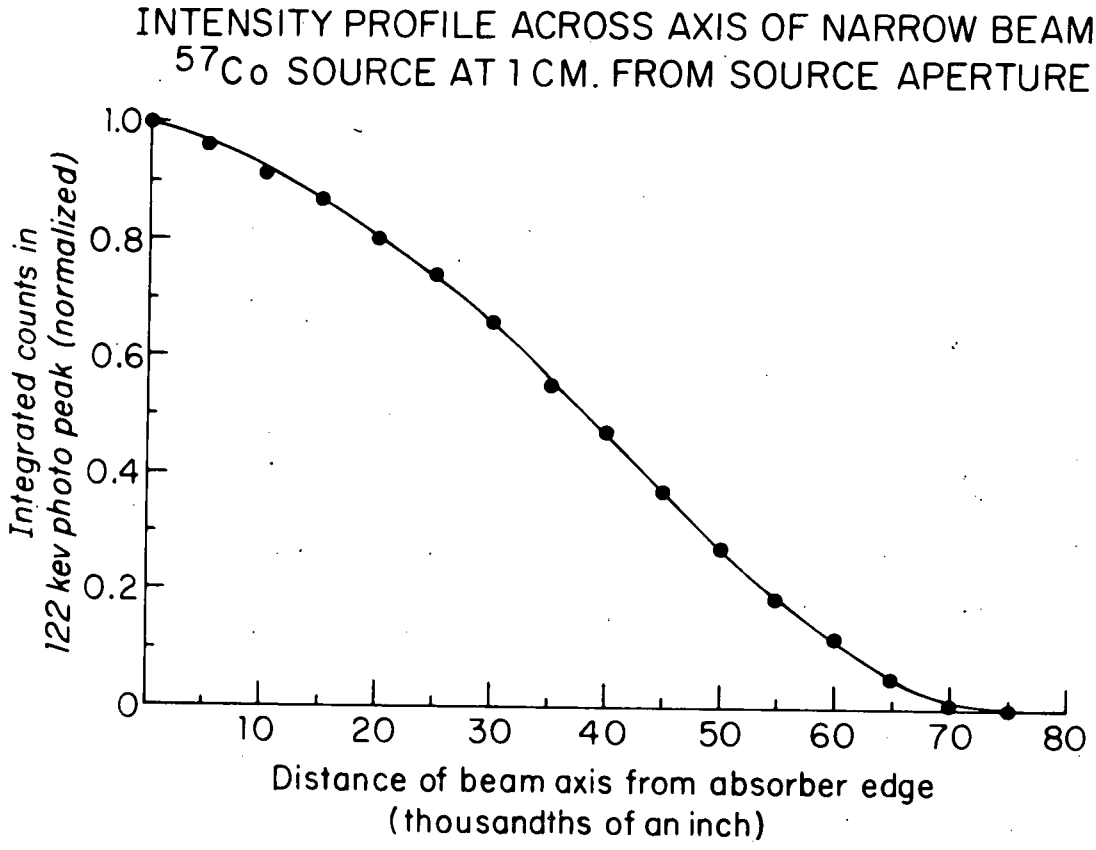

Figure 34. Intensity profile of narrow beam probe of ^{57}Co gamma rays.

used was the narrowly collimated one whose intensity profile appears in Figure (34). The ^{99m}Tc source was a pertechnetate solution provided by the Institute's Central Isotope Laboratory and was collimated to a 1 1/2mm beam through over an inch of collimator path. In all measurements the same fixed source to detector distance was used for both the germanium diode and the sodium iodide crystal. For ^{57}Co, including both the 122 keV and 136 keV lines, the photoelectric absorption efficiency of the diode was measured to be .64 relative to the sodium iodide crystal. The calculated first collision photoelectric efficiency for the 122 keV line is .62 while it is .49 for the 136 keV component. The measured photoelectric absorption efficiency of the diode for ^{99m}Tc was .51. The calculated value is .47.

D. Construction of a New Orthogonal Strip Matrix

Upon completion of the above tests, diode 2077-9 was formed into a 10 x 10 electrode strip matrix 3.25 cm on a side. The resulting device is shown in Figure (35) where the original (2 x 2)cm^2 ultra pure germanium matrix is shown next to it for comparison. In addition to almost a factor of 3 increase in area, the increase in absorber thickness (5mm compared to 8.7mm) will result in a significant improvement in gamma ray sensitivity. Initial tests performed at the writing of this report indicate that all electrode strips of the matrix are operating despite two unplanned openings of the cryostat due to a mechanical problem with the cryogenic system. Spectral resoltuion for ^{57}Co(122 keV) of 4 keV (FWHM) has been measured.

Tests required to characterize the image quality and ultimate stability of camera properties along with biological applications of the device will be complete before the end of the current contract year.

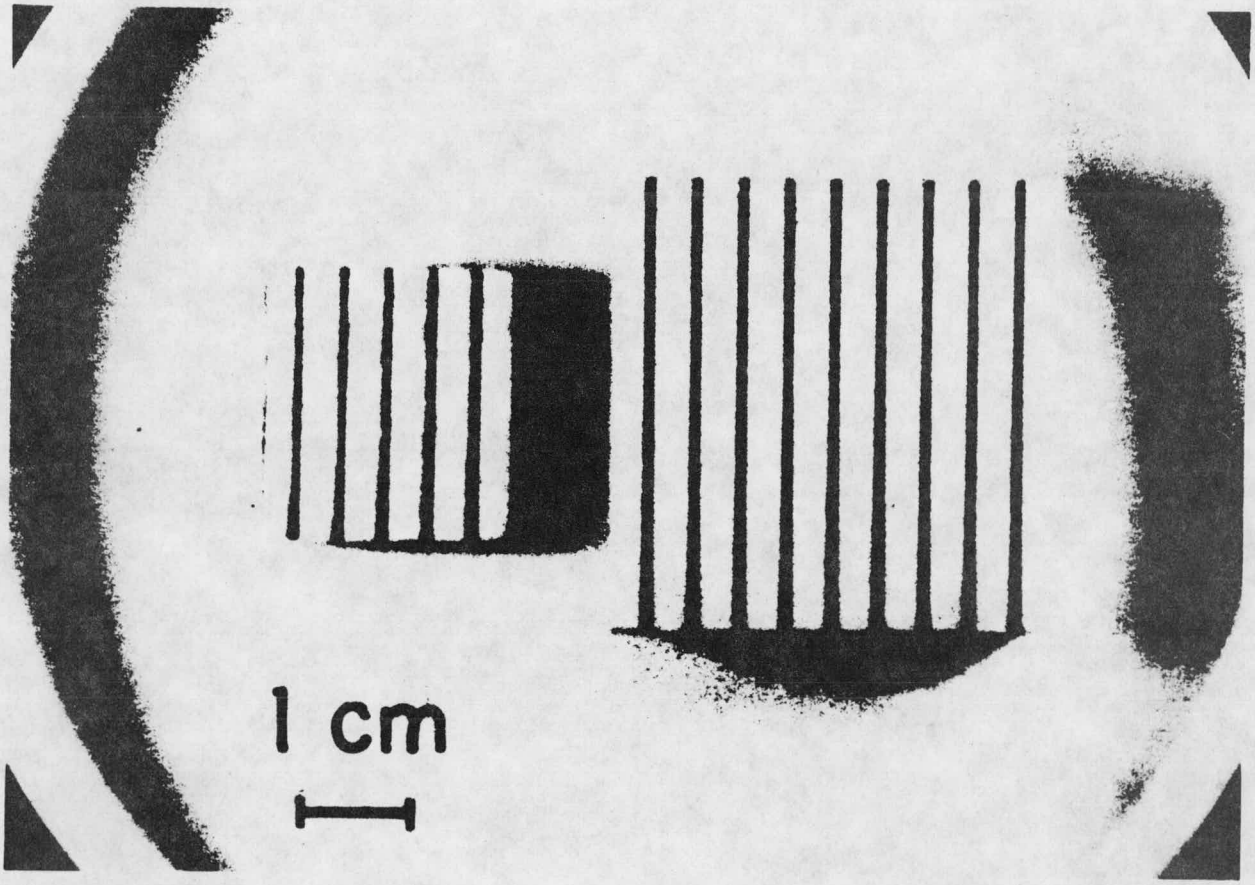

Figure 35. Photograph of new ultra pure germanium orthogonal strip matrix along with original (2 x 2) cm prototype matrix.

REFERENCES

1. Brennan, J.T. and Phillips, T.L., Evaluation of Past Experience with Fast Neutron Teletherapy and with Implications for Future Applications. Eur. J. of Cancer, 7: 219, (1971).

2. Bewley, D.K. and Parnell, C.J., The Fast Neutron Beam from the M.R.C. Cyclotron. Brit. J. Radiol., 42: 281, (1969).

3. Bruninx, E. and Crombeen, J., Thick Target Neutron Yields and Neutron Spectra Produced by 20 MeV Helium-3 Ions, 14 MeV Protons and 7.5 MeV Deuterons on a Beryllium Target. Int. J. Appl. Rad. and Isotopes, 20: 255, (1969).

4. Kuchnir, F.T., Skaggs, L.S., Elwyn, A.J., Mooring, F.P., Frigerio, N.A., Design of a Neutron Therapy Facility for a 30-inch Cyclotron, Cyclotrons-1972, American Institute of Physics, New York (1972).

5. ICRU (1964), Physical Aspects of Irradiation. ICRU Report 10b, International Commission on Radiation Units and Measurements, Washington, D.C. (NBS Handbook 85).

6. These treatment plans were calculated by L.D. Simpson of the MSKCC Medical Physics Department.

7. Barendsen, G.W., Walter, H.M.D., Fowler, J.F. and Bewley, D.K., Effects of Different Ionizing Radiations on Human Cells in Tissue Culture. Rad. Res., 18: 106, (1963).

8. Genna, S., Jaeger, R.G., Nagl, J. and Sanielevici, A. Quasi-Adiabatic Calorimeter for Direct Determination of Radiation Dose in Rads, Atomic Energy Rev., 1: 239, (1965).

9. Shonka, F.R., Rose, J.E. and Failla, G., Conducting Plastic Equivalent to Tissue, Air and Polystyrene, Prog. in Nuclear Energy, Series XII Vol. 1--Health Physics.

10. Anderson, L.L., Status of Dosimetry for ^{252}Cf Medical Neutron Sources, Medical Guidance Report to be issued by AEC Division of Biology and Medicine ^{252}Cf Biomedical Advisory Panel, U.S. Atomic Energy Commission, Savannah River Operations Office, Aiken, South Carolina, (1972).

11. Anderson, L.L., Dosimetry and Radiation Protection in ^{252}Cf Brachytherapy Programs. Phys. Med. Biol., 17: 682, (1972). Abstract.

12. Anderson, L.L. and Edelstein, G.R., Ion Chamber Dosimetry of ^{252}Cf Medical Neutron Source. Phys. Med. Biol., 17: 695, (1972). Abstract.

13. Djordjevic, B., Anderson, L.L. and Kim, S.H., Oxygen Enhancement Ratios in HeLa Cells Irradiated with Californium and Radium Sources. Radiology, 107: 429, (1973).

14. Hall, E.J., A Determination of the Oxygen Enhancement Ratio for ^{252}Cf Using Cultured Mammalian Cells. Brit. J. Radiol., 45: 284-288, (1972).

15. Hall, E.J., A Determination of the Oxygen Enhancement Ratio for ^{252}Cf Using Cultured Mammalian Cells. Brit. J. Radiol., 45: 628, (1972).

16. Annual Progress Report, Biological and Clinical Dosimetry, AEC Contract AT(30-1) 3522, pp. 13-18, (1971-72).

17. Detko, J.F., A Prototype Ultra Pure-Germanium Orthogonal Strip Gamma Camera. Medical Radioisotope Scintigraphy, Vol. 1, IAEA, pp. 241-254, (1973).

18. Annual Progress Report, Biological and Clinical Dosimetry, AEC Contract AT(30-1) 3510 (1967-68).

19. Detko, J.F., Semiconductor Diode Matrix for Isotope Localization. Phys. Med. Biol., Vol. 142, 245-253, (1969).

20. Baertsch, R.D., Collimated Beam Scanning of Pure Germanium Detectors. IEE Symposium, Miami, Dec., (1972).

21. Laughlin, J.S. and Genna, S., "Calorimetry", in Radiation Dosimetry (F.H. Attix and W.C. Roesch, eds.) Academic Press (1966) Chap. 16, pp. 389-441.

22. Hahn, E., Anderson, L.L. and Laughlin, J.S., Comparison of ^{252}Cf, Ra, and ^{60}Co effects on spermatogenesis in the rabbit, Abstract to be submitted to the R.S.N.A.

PUBLICATIONS AND PRESENTATIONS

Publications

Detko, J.F., Performance Characteristics of An Ultra-Pure Germanium Gamma Camera. Radiology. 104: 431-433, 1972.

Presentations

Canada, T.R., McDonald, J.C., Mittleman, A., and Laughlin, J.S., Neutron Dosimetry for a Compact Medical Cyclotron. 58th Scientific Assembly and Annual Meeting of the Radiological Society of North America, Work in Progress, Chicago, Nov. 26 - Dec. 1, 1972.

Laughlin, J.S., Canada, T.R., Simpson, L.D., McDonald, J.C., Kuo, T.Y.T., and Mittleman, A., Compact Cyclotron Neutron Dosimetry. The German-Austrian Roentgen Congress, Vienna, Austria, April 12-14, 1973.

Hahn, E.W., and McDonald, J.C., Embryogenesis in the Rat Following Fast Neutron Irradiation. Abstract (Ed-6), Annual Meeting of the Radiation Research Society, St. Louis, Missouri, April 29 - May 3, 1973.

Canada, T.R., McDonald, J.C., Mittleman, A., Kuo, T.Y.T., Freed, B.R., and Laughlin, J.S., Radiation Quality of Compact Cyclotron Produced Neutron Fields. Abstract (Ga-4), Annual Meeting of the Radiation Research Society, St. Louis, Missouri, April 29 - May 3, 1973.

Detko, J.F., A Prototype, Ultra-Pure Germanium, Orthogonal Strip Gamma Camera. Symposium on Medical Radioisotope Scintigraphy, Monte Carlo, Monaco, Oct. 1972. (In Press).

Detko, J.F., Operational Characteristics of a Small Ultra-Pure Germanium Gamma Camera, Semiconductor Detectors in Medicine, San Francisco, Calif., March 1973. (In Press).